Cell Reports

Article

# Circuit-selective cell-autonomous regulation of inhibition in pyramidal neurons by Ste20-like kinase

## Graphical abstract

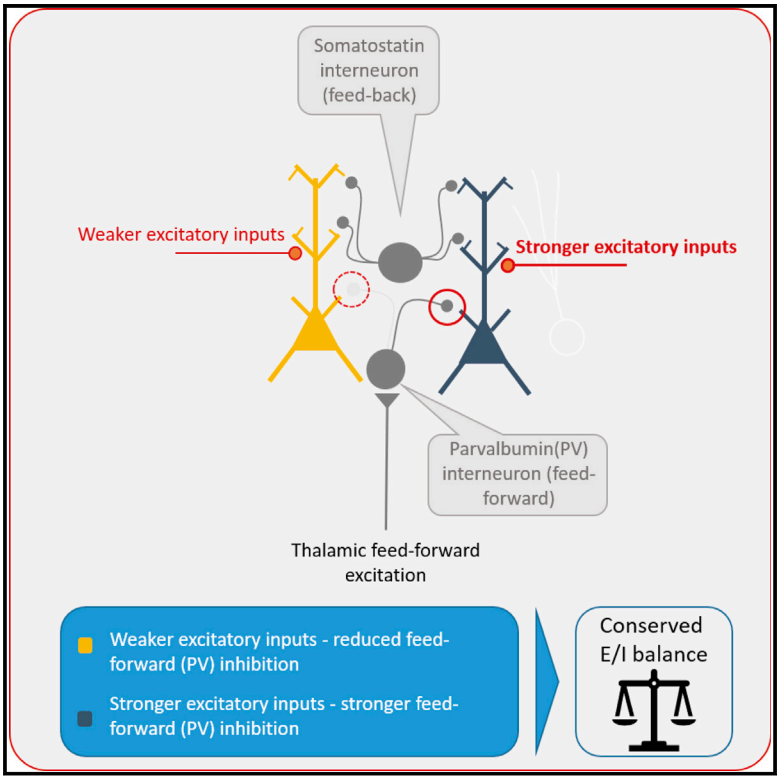


## Highlights

- SLK regulates excitation-inhibition balance cell-autonomously
- SLK in cortical neurons regulates feedforward but not feedback inhibition
- SLK selectively regulates inhibition by parvalbumin-expressing interneurons


## Authors

Pedro Royero, Anne Quatraccioni, Rieke Früngel, ..., Albert Becker, Susanne Schoch, Heinz Beck

## Correspondence

heinz.beck@ukbonn.de



## In brief

Royero et al. identify a mechanism relying on Ste20-like kinase that allows single cortical neurons to cell-autonomously adjust feedforward inhibition they receive to the cell-specific levels of excitatory input. They propose that this mechanism is critical to ensure that a majority of cortical pyramidal cells participate in information coding.


Royero et al., 2022, Cell Reports *41*, 111757
December 6, 2022 
https://doi.org/10.1016/j.celrep.2022.111757

CellPress

Cell Reports

CellPress
OPEN ACCESS

Article

# Circuit-selective cell-autonomous regulation of inhibition in pyramidal neurons by Ste20-like kinase

Pedro Royero,[1,9] Anne Quatraccioni,[2,9] Rieke Früngel,[3,9] Mariella Hurtado Silva,[10] Arco Bast,[3,9] Thomas Ulas,[4,5,7] Marc Beyer,[5,6] Thoralf Opitz,[1] Joachim L. Schultze,[4,5,7] Mark E. Graham,[1] Marcel Oberlaender,[3] Albert Becker,[2] Susanne Schoch,[2] and Heinz Beck[1,8,11,*]

[1]Institute of Experimental Epileptology and Cognition Research, University of Bonn, University of Bonn Medical Center, Venusberg-Campus 1, 53105 Bonn, Germany
[2]Department of Neuropathology, University Hospital Bonn, Section for Translational Epilepsy Research, 53127 Bonn, Germany
[3]In Silico Brain Sciences Group, Max-Planck Institute for Neurobiology of Behavior – Caesar, Bonn, Germany
[4]Systems Medicine, Deutsches Zentrum für Neurodegenerative Erkrankungen (DZNE) e.V., Bonn, Germany
[5]PRECISE Platform for Single Cell Genomics and Epigenomics, Deutsches Zentrum für Neurodegenerative Erkrankungen (DZNE) e.V. and University of Bonn, Bonn, Germany
[6]Immunogenomics & Neurodegeneration, Deutsches Zentrum für Neurodegenerative Erkrankungen e.V., Bonn, Germany
[7]Genomics & Immunoregulation, LIMES Institute, University of Bonn, Bonn, Germany
[8]Deutsches Zentrum für Neurodegenerative Erkrankungen e.V., Bonn, Germany
[9]International Max Planck Research School for Brain and Behavior, Bonn, Germany
[10]Synapse Proteomics, Children's Medical Research Institute, The University of Sydney, Sydney, NSW, Australia
[11]Lead contact
*Correspondence: heinz.beck@ukbonn.de
https://doi.org/10.1016/j.celrep.2022.111757

## SUMMARY

Maintaining an appropriate balance between excitation and inhibition is critical for neuronal information processing. Cortical neurons can cell-autonomously adjust the inhibition they receive to individual levels of excitatory input, but the underlying mechanisms are unclear. We describe that Ste20-like kinase (SLK) mediates cell-autonomous regulation of excitation-inhibition balance in the thalamocortical feedforward circuit, but not in the feedback circuit. This effect is due to regulation of inhibition originating from parvalbumin-expressing interneurons, while inhibition via somatostatin-expressing interneurons is unaffected. Computational modeling shows that this mechanism promotes stable excitatory-inhibitory ratios across pyramidal cells and ensures robust and sparse coding. Patch-clamp RNA sequencing yields genes differentially regulated by SLK knockdown, as well as genes associated with excitation-inhibition balance participating in transsynaptic communication and cytoskeletal dynamics. These data identify a mechanism for cell-autonomous regulation of a specific inhibitory circuit that is critical to ensure that a majority of cortical pyramidal cells participate in information coding.

## INTRODUCTION

All cortical processing is critically influenced by the temporal and spatial interplay of synaptic excitation and inhibition. The nature of this interplay in the brain is determined by the circuit architecture linking excitatory and inhibitory neurons,[1] with feedforward and feedback inhibition being the most fundamental circuits.[2,3] In the cortex, sensory stimulation gives rise to activation of thalamocortical inputs,[4] which not only impinge onto excitatory neurons but also recruit inhibitory feedforward interneurons (INs).[5–7] Conversely, the activity of cortical excitatory neurons recruits local GABAergic INs, which then provide feedback inhibition within the same cortical area. The strong circuit-based links between excitation and inhibition cause global temporal correlations between cortical excitation and inhibition because increases in excitation always cause commensurate increases in inhibition across cortical neurons.[1]

At the level of individual cells, however, adjacent cortical neurons receive widely differing excitatory input strengths, both from neighboring neurons[8] and thalamocortical inputs.[9] Despite this variability, the balance of excitation and inhibition was shown to be remarkably stable across individual cortical neurons.[10,11] This implies a high degree of correlation in each individual cortical neuron between excitation and inhibition and requires a mechanism by which neurons can individually adjust the inhibition they receive to the excitatory input strength.[12] Nonetheless, the cellular mechanisms governing cell-autonomous regulation of inhibition are insufficiently understood.

Here, we describe a cell-intrinsic mechanism underlying such a regulation that involves Ste20-like kinase (SLK), a highly

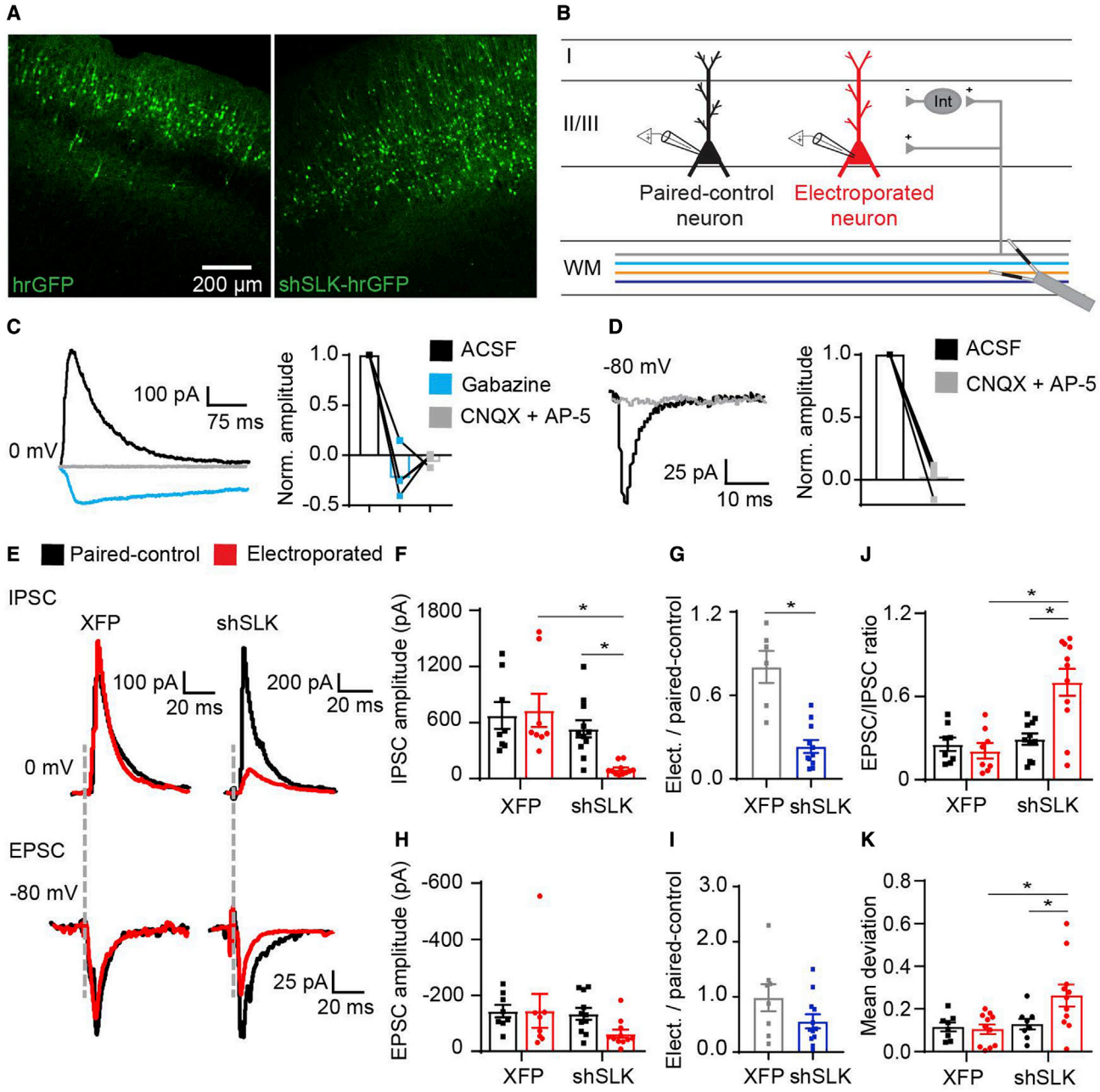


**Figure 1. Neurons with reduction in SLK levels display a deficit in synaptic inhibition**

(A) Representative micrograph of neurons expressing hrGFP in mice *in utero* electroporated at E14 either with only the fluorescent protein (XFP) or with SLK-shRNA-hrGFP (shSLK) plasmids.

(B) Schematic of the experiment depicting recording from both electroporated pyramidal neurons in layer II/III (either control XFP or shSLK) and non-electroporated neighboring neurons (paired-control PC). Postsynaptic currents were evoked by stimulating the subcortical white matter with a bipolar electrode.

(C) Representative IPSCs recorded at 0 mV to minimize the contribution of glutamatergic transmission. Large outward currents were blocked by gabazine (10 µM, blue traces). PSCs were completely blocked by additional application of CNQX and D-AP5 (50 and 200 µM, respectively, gray traces).

(D) Representative EPSCs elicited with electrical stimulation while holding neurons at −80 mV. EPSCs were blocked by the combined application of CNQX and D-AP5 (gray traces).

(E) Representative examples of IPSCs (upper traces) and EPSCs (lower traces) in electroporated XFP and shSLK neurons (red traces), and adjacent paired-control PCs in the same slice preparation (black traces). Dashed gray lines indicate the time point when the electrical stimulation was applied.

(F and H) Comparison of evoked IPSC (F) and EPSC (H) amplitudes in neurons expressing shSLK (number of pairs = 11) or control XFP (number of pairs = 8) compared with their respective, adjacent paired-control pyramidal neurons. IPSCs (F): two-way repeated measures ANOVA main effects, XFP versus shSLK:

*(legend continued on next page)*

conserved mammalian member of the Ste20/Hippo kinase family that has been implicated in cytoskeletal dynamics and, more recently, inhibitory synapse maintenance.[13,14] This mechanism allows individual cortical pyramidal neurons to regulate selectively the amount of feedforward inhibition impinging on it while leaving feedback inhibition unaffected. We further show that this adaptation relies on the regulation of inhibition through parvalbumin (Pv)-expressing INs, but not somatostatin (SST)-expressing INs, and allows cell-autonomous regulation of excitation-inhibition balance.

## RESULTS

### Altered synaptic excitation-inhibition balance in SLK-deficient neurons

It has been described previously that SLK regulates the maintenance of GABAergic synapses in cortical neurons.[14] To examine if decreased SLK expression also affects inhibition in cortical circuits, we examined stimulation-evoked inhibitory and excitatory transmission. We obtained brain slices from mice *in utero* electroporated at E14 either with control fluorescent protein (XFP; in this case hrGFP) or SLK-shRNA-hrGFP (shSLK) plasmids (Figures 1A and 1B). We recorded from hrGFP-expressing layer II/III pyramidal cells (PCs), as well as from at least one immediately adjacent PC not targeted by the electroporation in the same slice (paired-control PCs, Figure 1B). We then evoked excitatory and inhibitory postsynaptic currents (EPSCs and IPSCs) by stimulation of the subcortical white matter. We assessed the IPSC amplitude by holding neurons at 0 mV, resulting in $GABA_A$ receptor-mediated outward currents that were blocked by gabazine (Figure 1C, 10 μM). EPSCs were recorded by holding neurons at −80 mV, close to the reversal potential of IPSCs, resulting in PSCs entirely blocked by the combined application of CNQX and D-AP5 (Figure 1D, 50 and 200 μM).

We found a significant reduction in the amplitude of evoked IPSCs in neurons expressing shSLK compared with adjacent paired-control PCs, and cells electroporated with control XFP (Figures 1E–1G, two-way repeated measures ANOVA and Bonferroni's post-test, shSLK versus paired-control $p = 0.008$; shSLK versus XFP $p < 0.001$). If the amount of IPSC reduction was expressed as a ratio to the adjacent paired-control PC, the IPSCs were strongly reduced in the shSLK neurons (Figure 1G, XFP and shSLK 80% and 23% of paired-control IPSCs, respectively, Mann-Whitney U test, $p = 0.001$). In contrast, stimulation-evoked EPSCs did not show a significant reduction in neurons expressing shSLK (Figure 1H, two-way repeated measures ANOVA). Moreover, we did not find changes in the presynaptic release probability in excitatory inputs onto SLK-deficient neurons after repetitive electrical stimulation (Figure S1).

Measuring EPSC and IPSC magnitudes in the same neuron allowed us to compute a ratio between excitatory and inhibitory inputs for each cell. As expected, the excitation-inhibition balance was significantly shifted in SLK-deficient neurons (Figure 1J, two-way ANOVA, Bonferroni's post-test, shSLK versus paired-control $p < 0.001$; shSLK versus XFP $p < 0.001$). Previous studies have shown that inhibition can be precisely adjusted to the levels of excitation cortical neurons receive, resulting in remarkably constant excitation-inhibition balance across individual cortical neurons.[11] We therefore tested if SLK loss also affects the variability of excitatory-inhibitory ratios. Indeed, SLK-deficient neurons displayed significantly increased variability in EPSC/IPSC ratios compared with control neurons (Figure 1K, Levene's test for equality of variances, $F_{(3,34)} = 4.869$, $p = 0.0064$; Holm-Sidak's multiple comparisons test, shSLK versus paired-control $p = 0.0104$; shSLK versus XFP $p = 0.0476$). Thus, decreasing SLK expression leads to a selective loss of circuit-based inhibition, but also a loss of precision in the tuning of excitation-inhibition balance in pyramidal neurons.

### SLK deficiency causes abnormal excitation-inhibition balance in a feedforward circuit

Inhibition in the cortex is organized into feedforward and feedback motifs.[1–3] We elucidated if the deficit in inhibition impinges on only one or both of these inhibitory motifs. We first examined feedforward inhibition using an optogenetic approach. We expressed ChR2 in the thalamus with AAV-mediated gene transfer. We used injection coordinates targeting thalamocortical neurons that project to cortical areas overlapping the IUE-affected area (Figure S2A; see STAR Methods). Following the injection, we identified large numbers of ChR2-eYFP-expressing axons in layer IV, as expected for primary thalamic afferents,[15] as well as in layer I, where afferents from higher-order thalamus terminate[16] (Figure 2A). We discriminated EPSC from IPSC components as in Figure 1 (Figures 2C and 2D). Light-evoked IPSCs, but not EPSCs were blocked after the combined application of tetrodotoxin and 4-aminopyridine (1 and 200 μM). This indicates that IPSCs are disynaptic, and result from feedforward activation of INs by thalamic inputs, whereas EPSCs are largely monosynaptic (Figures 2E and 2F). In the experimental group in which electroporated neurons lack SLK protein, a substantial reduction of both IPSCs (Figures 2G–2I, two-way repeated measures ANOVA, Bonferroni's post-test, shSLK versus paired-control $p < 0.001$; shSLK versus XFP $p = 0.009$) and EPSCs was

$F_{(1,17)} = 10.15$, $p = 0.005$; electroporated versus paired-control: $F_{(1,17)} = 3.519$, $p = 0.078$; interaction: $F_{(1,17)} = 5.846$, $p = 0.027$; asterisks indicate Bonferroni's post-test, shSLK versus paired-control $p = 0.008$; shSLK versus XFP $p < 0.001$). EPSCs (H): two-way repeated measures ANOVA, $F_{(1,17)} = 1.7$, $p = 0.214$.

(G) Ratio of IPSCs in XFP or shSLK neurons expressed as a fraction of IPSCs recorded in adjacent paired-control PC. Asterisk indicates Mann-Whitney U test, $p = 0.001$.

(I) As in (G), ratios computed for EPSCs.

(J) Excitation-inhibition balance computed as the EPSC/IPSC ratio for each individual XFP or shSLK (red) and the respective paired-control PC (black). Two-way ANOVA, XFP versus shSLK: $F_{(1,34)} = 14.58$, $p < 0.001$; electroporated versus paired-control $F_{(1,34)} = 6.81$, $p = 0.013$; interaction: $F_{(1,34)} = 10.81$, $p = 0.002$; Asterisks indicate Bonferroni's post-test, shSLK versus paired-control $p < 0.001$; shSLK versus XFP $p < 0.001$).

(K) Mean deviation of the EPSC/IPSC ratio for each individual XFP or shSLK neuron (red) and the respective paired-control PC (black). Levene's test for equality of variances, $F_{(3,34)} = 4.869$, $p = 0.0064$; asterisks indicate Holm-Sidak's multiple comparisons test, shSLK versus paired-control $p = 0.0104$; shSLK versus XFP $p = 0.0476$). Data are represented as mean ± SEM.

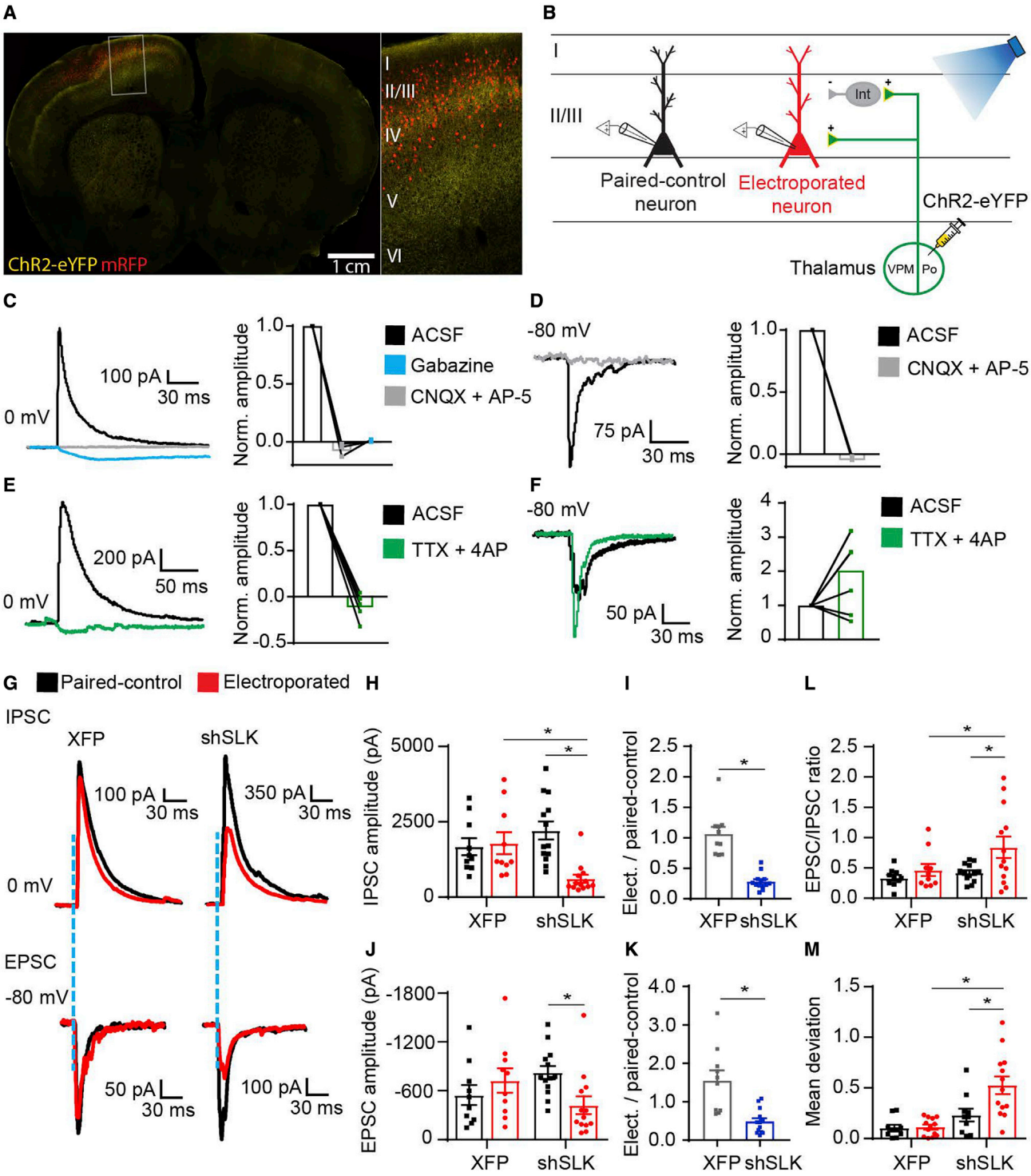


**Figure 2. Abnormal excitation-inhibition balance in SLK-deficient neurons resides in a feedforward circuit**

(A) Representative micrograph of cortical electroporated neurons and ChR2-eYFP-expressing thalamic axons reaching the electroporated area.

(B) Schematic of the experiment. ChR2-eYFP was expressed through stereotactic injections in thalamic nuclei projecting to M1 and S1. Patch-clamp recordings were carried out from both electroporated pyramidal neurons in layer II/III (either control XFP or shSLK) and non-electroporated neighboring neurons (paired-control PCs).

(C) Representative light-evoked IPSCs recorded at 0 mV to minimize the contribution of glutamatergic transmission. Large outward currents were blocked by gabazine (10 μM, blue traces). PSCs were completely blocked by additional application of CNQX and D-AP5 (50 and 200 μM, respectively, gray traces).

*(legend continued on next page)*

observed compared with adjacent control neurons (Figures 2G, 2J, and 2L, two-way repeated measures ANOVA, Bonferroni's post-test, shSLK versus paired-control $p < 0.001$). This finding was stable over a large range of optogenetic stimulation intensities (Figures S2B and S2C).

This striking finding resulted in significant differences between control and experimental animals. Even though both EPSCs and IPSCs were significantly reduced, inhibition was reduced to a greater extent. As a consequence, excitation-inhibition balance was significantly elevated in SLK-deficient neurons (Figure 2L, Bonferroni's post-test, shSLK versus paired-control $p = 0.015$; shSLK versus XFP $p = 0.050$). Moreover, the variability of EPSC/IPSC ratios in SLK-deficient neurons was also increased (Figure 2M, Levene's test for equality of variances, $F_{(3,42)} = 11.82$, $p < 0.0001$; Holm-Sidak's multiple comparisons test, shSLK versus paired-control $p < 0.0001$; shSLK versus XFP $p = 0.005$). Consistent with the results in Figure 1, this indicates a loss of precise tuning of excitation-inhibition balance in a feedforward circuit targeting SLK-deficient pyramidal neurons.

### Inhibition supplied by cortical feedback circuits is unaltered in SLK-deficient neurons

To assess feedback inhibition, we expressed ChR2 in adjacent excitatory cortical cells using a dual viral approach (Figures 3A and 3B, injection of a virus expressing Cre-recombinase under a CaMKII promoter only in excitatory neurons, in addition to a virus conditionally expressing ChR2; see STAR Methods). In electroporated neurons, blue light stimulation evoked PSCs that could be separated into component EPSCs and IPSCs by clamping to different holding potentials as in Figures 1 and 2 (Figures 3C and 3D). A long light pulse of 500 ms was applied to determine whether patched cells expressed ChR2 (Figure S3A). Direct photocurrents were observed in only 3 of 35 electroporated neurons, which were excluded from further analysis.

Surprisingly, neither IPSC (Figures 3E–3G) nor EPSC amplitudes (Figures 3E, 3H, and 3I, two-way repeated measures ANOVA, n.s.) were affected in shSLK versus adjacent non-electroporated or versus XFP layer II/III PCs. As a consequence, the magnitude (Figure 3J, two-way ANOVA, n.s.) and variance (Figure 3K, Levene's test for equality of variances, n.s.) of the excitation-inhibition ratio evoked in feedback circuits were unchanged in SLK-deficient neurons. This surprising finding indicates that the inhibitory deficit and deficient tuning of excitation-inhibition balance mainly affect feedforward inhibition, and do not seem to affect feedback or lateral inhibitory circuits.

### Timing of inhibition is altered in shSLK neurons

Feedforward inhibition is normally fast and synchronous, due to the strong and fast excitation of feedforward INs, mainly of Pv-expressing Ins.[7] We therefore examined if the strong reduction of feedforward inhibition is associated with altered timing of inhibition. In optogenetic experiments in which we stimulated thalamocortical axons, the remaining small residual IPSCs in shSLK neurons displayed a significantly slower rate of increase compared with paired control cells (two-way repeated measures ANOVA, Bonferroni's post-test, shSLK versus paired-control $p < 0.001$; shSLK versus XFP $p < 0.001$, Figures S4A and S4B) without effects on the IPSC decay (Figure S4C). No changes were observed in monosynaptic feedforward thalamocortical EPSCs (Figures S5A–S5C). Similar changes in IPSCs were seen following electrical stimulation of the white matter. In this stimulation paradigm, which recruits feedforward, but also other forms of cortical inhibition, IPSCs also showed a delayed time course in shSLK neurons (Figures S5D–S5F). In contrast, the timing of feedback inhibition was not altered, consistent with the idea that this form of inhibition is not changed in SLK-deficient neurons (Figures S5J–S5L). These data indicate a pronounced change in the amount and timing of inhibition in a thalamocortical feedforward circuit.

(D) Representative EPSCs elicited by blue light-based stimulation of thalamic axons while holding neurons at −80 mV. EPSCs were blocked by the combined application of CNQX and D-AP5 (gray traces).

(E and F) Light-evoked IPSCs were disynaptic, while EPSCs were monosynaptic. IPSCs are completely blocked after the application of tetrodotoxin and 4-aminopyridine (TTX/4-AP, 1 and 200 μM) (E). EPSCs persist after combined application of TTX/4-AP due to direct optogenetic stimulation of glutamatergic terminals onto layer II/III pyramidal neurons (F).

(G) Representative examples of light-evoked IPSCs (upper traces) and EPSCs (lower traces) in electroporated XFP and shSLK neurons (red traces), and adjacent paired-control PCs in the same slice preparation (black traces). Dashed blue lines indicate the time point when the light-based stimulation was applied.

(H and J) Comparison of light-evoked IPSCs (H) and EPSCs (J) in neurons expressing shSLK (number of pairs = 13) or control XFP (number of pairs = 10) compared with their respective, adjacent paired-control pyramidal neurons. IPSCs (H): two-way repeated measures ANOVA, main effects XFP versus shSLK: $F_{(1,21)} = 0.803$, $p = 0.380$; electroporated versus paired-control: $F_{(1,21)} = 21.98$, $p < 0.001$; interaction: $F_{(1,21)} = 29.33$, $p < 0.001$; Bonferroni's post-test, shSLK versus paired-control $p < 0.001$; shSLK versus XFP $p = 0.009$. EPSCs (J): two-way repeated measures ANOVA, main effects XFP versus shSLK $F_{(1,21)} = 0.008$, $p = 0.931$; electroporated versus paired-control $F_{(1,21)} = 2.65$, $p = 0.119$; interaction: $F_{(1,21)} = 17.9$, $p < 0.001$; Bonferroni's post-test, shSLK versus paired-control $p < 0.001$.

(I) Ratio of light-evoked IPSCs in XFP or shSLK neurons expressed as a fraction of IPSCs recorded in adjacent paired-control PCs. Asterisk indicates Mann-Whitney U test, $p < 0.0001$.

(K) As in (G), ratios computed for EPSCs. Asterisk indicates Mann-Whitney U test, $p < 0.001$.

(L) Excitation-inhibition balance computed as the EPSC/IPSC ratio for each individual XFP, shSLK (red), and their respective paired-control PCs (black). Two-way ANOVA, main effects XFP versus shSLK: $F_{(1,42)} = 4.072$, $p = 0.050$; electroporated versus paired-control: $F_{(1,42)} = 5.828$, $p = 0.020$; interaction: $F_{(1,42)} = 1.624$, $p = 0.210$; Asterisks indicate Bonferroni's post-tests. shSLK versus paired-control $p = 0.015$; shSLK versus XFP $p = 0.050$.

(M) Mean deviation of the EPSC/IPSC ratio for each individual XFP or shSLK neuron (red) and the respective paired-control PC (black). Asterisks indicate post-tests following Levene's test for equality of variances. Holm-Sidak's multiple comparisons test shSLK versus paired-control $p < 0.0001$; shSLK versus XFP $p = 0.005$. Data are represented as mean ± SEM.

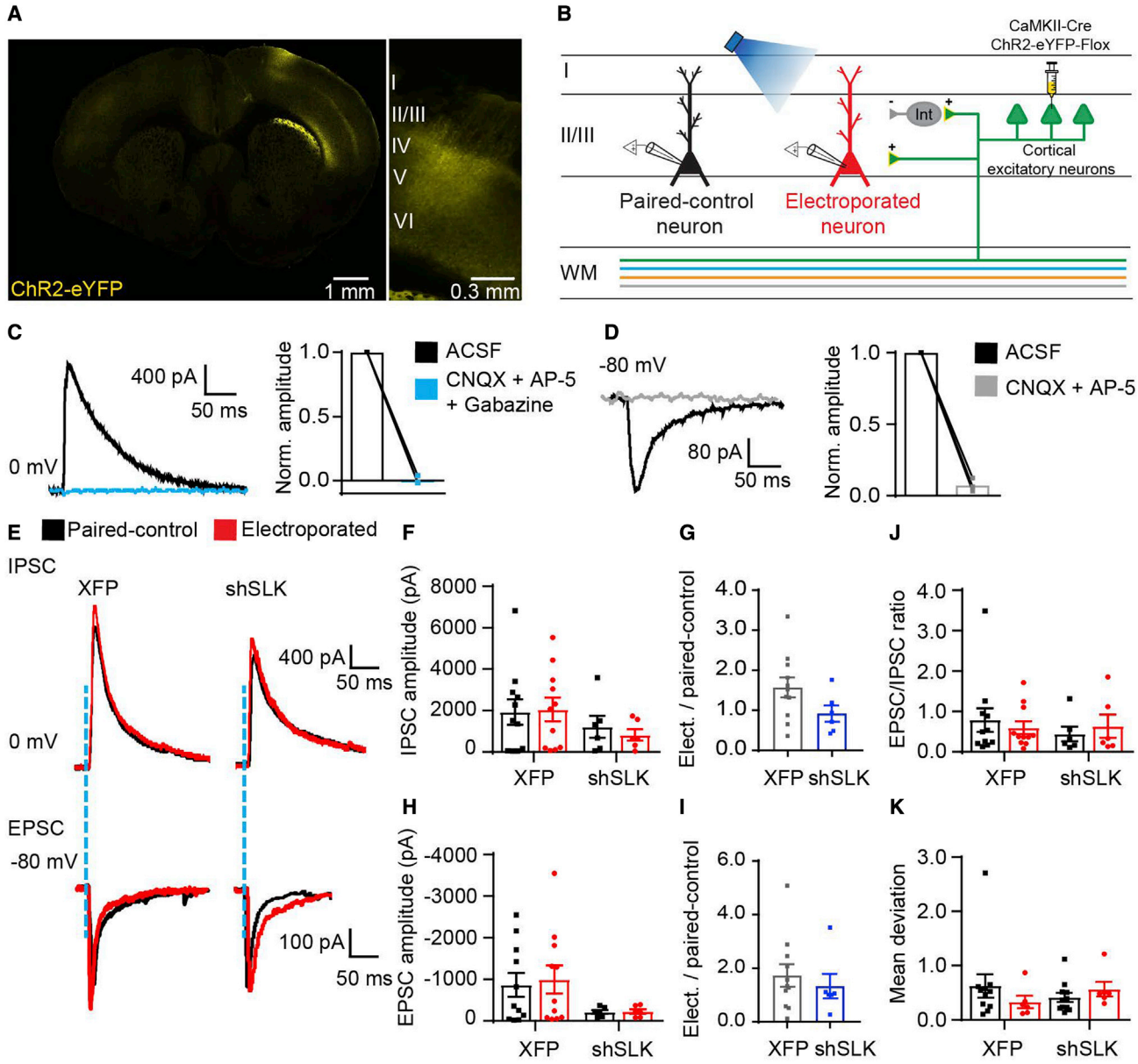


**Figure 3. SLK-KD neurons do not show changes in feedback inputs**

(A) Representative micrograph of ChR2-eYFP-expressing axons of cortical excitatory neurons virally transduced with Cre-recombinase under a CaMKII promoter and Cre-conditional ChR2.

(B) Schematic of the experiment. ChR2 was expressed in cortical layer II/III excitatory neurons. Patch-clamp recordings were carried out from both electroporated pyramidal neurons in layer II/III (either control XFP or shSLK) and non-electroporated neighboring neurons (paired-control PCs).

(C) Light-evoked IPSCs recorded at 0 mV to minimize the contribution of glutamatergic transmission in ACSF and after the combined application of CNQX, D-AP5, and gabazine (50, 200, and 10 μM respectively, blue traces).

(D) Representative EPSCs elicited by blue light-based stimulation of cortical neurons while holding neurons at −80 mV. Gray traces indicate the application of CNQX and D-AP5 (50 and 200 μM, respectively).

(E) Representative examples of light-evoked IPSCs (upper traces) and EPSCs (lower traces) in electroporated XFP and shSLK neurons (red traces), and adjacent paired-control neurons in the same slice preparation (black traces). Dashed blue lines indicate the time point when the light-based stimulation was applied.

(F and H) Comparison of light-evoked IPSCs (F) and EPSCs (H) in neurons expressing shSLK (number of pairs = 6) or control XFP (number of pairs = 11) compared with their respective, adjacent paired-control pyramidal neurons.

(G and I) Ratio of light-evoked IPSCs (G) or EPSCs (I) in XFP or shSLK neurons expressed as a fraction of IPSCs recorded in adjacent paired-control PCs.

(J) Excitation-inhibition balance computed as the EPSC/IPSC ratio for each individual XFP, shSLK (red), and the respective paired-control neurons (black).

(K) Mean deviation of the EPSC/IPSC ratio for each individual XFP or shSLK (red) neuron and the respective paired-control PC (black). Data are represented as mean ± SEM.

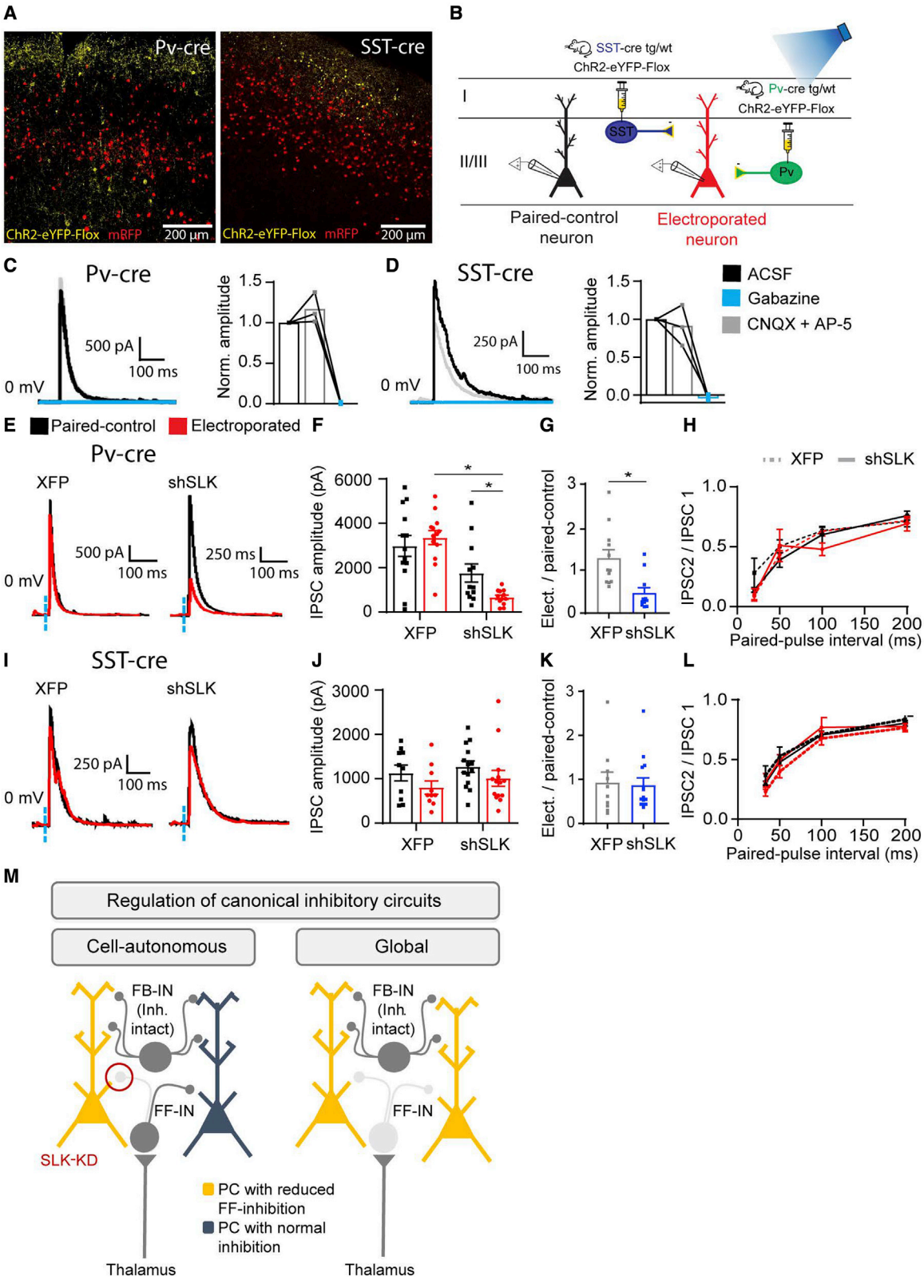


*(legend on next page)*

### Inhibition mediated by Pv-expressing INs and not by SST-expressing INs is reduced in SLK-deficient neurons

Once we determined that SLK-deficient neurons display a profound inhibition impairment constrained to feedforward circuits, we addressed if a specific IN subtype is responsible for the excitatory-inhibitory imbalance observed after thalamic activation. The distribution of thalamic inputs differs across distinct GABAergic neuron types in cortical areas, preferentially recruiting Pv-expressing over SST-expressing INs in the somatosensory cortex.[7] To measure inhibitory inputs from either IN type onto SLK-deficient cells, we expressed ChR2-eYFP in Pv- or SST-expressing neurons using AAV-mediated gene transfer in Pv- or SST-Cre mice, respectively (Figures 4A and 4B). Two weeks after injection, selective ChR2-eYFP was detected in Pv- and SST-INs, which reliably displayed direct photocurrents and action potentials after blue light stimulation (Figures S6A–S6F). Light-evoked PSCs recorded in electroporated PCs were unaffected by the addition of CNQX and D-AP5 (50 and 200 μM) to the recording chamber but completely blocked after perfusing gabazine (10 μM), indicating that light-evoked responses originate only from GABAergic INs (Figures 4C and 4D). Immunostaining analysis revealed that there are no changes in the number of Pv- and SST-INs in SLK-KD animals (Figures S6G–S6J).

We then assessed the inhibitory responses following light-based stimulation of Pv-INs in both SLK-deficient pyramidal neurons and paired-control cells in the same slice preparation. Neurons electroporated with shSLK plasmids showed a large reduction in IPSC amplitudes, compared with paired-control cells and neurons electroporated only with control XFP (Figures 4E–4G, two-way ANOVA, Bonferroni's post-test, shSLK versus paired-control $p = 0.0442$; shSLK versus XFP $p < 0.001$). These findings were stable over a large range of optogenetic stimulation intensities and holding potentials (Figures S7A and S7B). In contrast, no differences were observed in SST-mediated IPSC amplitudes (Figures 4I–4K, two-way repeated measures ANOVA, n.s., Figures S7E–S7H).

This selective loss of inhibition by Pv-INs could be due to a loss of specific inhibitory sites on SLK-deficient neurons, but it could also be due to presynaptic changes. To address this possibility, we performed paired-pulse experiments. We found no differences in either Pv- or SST-IN paired-pulse ratio in shSLK electroporated neurons compared with paired-control cells and neurons electroporated with control XFP (Figures 4H and 4L). These results indicate that it is unlikely that changes in presynaptic release probability at the Pv-pyramidal neuron synapses contribute to the loss of inhibition.

Collectively, the results so far suggest that SLK in cortical neurons mediates cell-autonomous regulation of inhibition in the thalamocortical feedforward circuit, but not in the feedback circuit, and that this effect is due to regulation of inhibition originating from Pv-expressing INs (see schematic in Figure 4M).

### shSLK neurons exhibit increased c-fos expression indicative of increased activity

The marked effect of SLK-KD on feedforward inhibition predicts that sensory recruitment of these neurons occurs with a pronounced deficit in inhibition, suggesting that they may be hyperactive in intact animals. We tested this idea using c-fos labeling, a technique that is useful to screen for general changes in the levels of activity. We assessed c-fos immunolabeling in electroporated cells in animals that received control plasmids containing only hrGFP (Figure 5A), and in animals electroporated with shSLK-hrGFP (Figure 5B). The number of hrGFP expressing cells that also expressed c-fos was significantly increased in shSLK electroporated animals (Figure 5C, unpaired t test, $t_{(21)} = 3.38$, $p = 0.0028$). Likewise, the c-fos fluorescence intensity measured in the somatic area of hrGFP-expressing cells was markedly decreased. Thus, SLK-deficient neurons seem to constitute a more active cell population compared with control neurons, consistent with the overall loss of inhibition.

We did not observe increased c-fos staining in areas remote from the cortex affected by the electroporation (prefrontal cortex, contralateral somatosensory cortex, and hippocampus,

**Figure 4. Inhibition supplied by Pv-interneurons is selectively reduced in SLK-deficient neurons**

(A) ChR2-eYFP expression in Pv (left) and SST (right) INs in cortical slices electroporated with mRFP.

(B) Schematic of the experiment. Patch-clamp recordings were carried out from both electroporated pyramidal neurons in layer II/III (either control XFP or shSLK) and non-electroporated neighboring neurons (paired-control PCs) from acute brain slices of Pv- and SST-Cre animals.

(C and D) Representative IPSCs elicited by blue light-based stimulation of Pv- (C) and SST-expressing INs (D) while applying a holding voltage of 0 mV. IPSCs were unaffected by the combined application of CNQX and D-AP5 (50 and 200 μM, respectively, gray traces), but completely blocked by the application of gabazine (10 μM, blue traces).

(E and I) Representative examples of light-evoked IPSCs in Pv- (E) and SST-Cre (I) animals of electroporated XFP and shSLK neurons (red traces), and adjacent paired-control neurons in the same slice preparation (black traces).

(F and J) Comparison of light-evoked IPSCs in Pv- (F) and SST-Cre (J) animals of neurons expressing shSLK (number of pairs: Pv = 11, SST = 14) or control XFP (number of pairs: Pv = 12, SST = 10) compared with their respective, adjacent paired-control pyramidal neurons. (F) Pv-Cre: two-way repeated measures ANOVA, main effects XFP versus shSLK: $F_{(1,23)} = 23.44$, $p < 0.001$; electroporated versus paired-control: $F_{(1,23)} = 1.34$, $p = 0.259$; interaction: $F_{(1,23)} = 5.67$, $p = 0.0259$; asterisks indicate Bonferroni's post-test, shSLK versus paired-control $p = 0.0442$; shSLK versus XFP $p < 0.001$).

(G and K) Ratio of light-evoked IPSCs in Pv- (G) and SST-Cre (K) animals of XFP or shSLK neurons expressed as a fraction of IPSCs recorded in adjacent paired-control pyramidal neurons. Asterisk indicates Mann-Whitney U test, Pv-Cre (G) $p = 0.0013$.

(H and L) Paired-pulse ratio (faction of second to first response) recorded in electroporated and paired-control excitatory neurons after light-based activation of Pv- (H) and SST-expressing INs (L). There were no differences between groups across any of the frequency stimulation performed. Data are represented as mean ± SEM.

(M) Schematic of cell-autonomous and global regulation of canonical inhibitory motifs. In this example, the regulated motif is feedforward inhibition. Pyramidal cells affected by modulated feedforward inhibition are designated in yellow. FB-IN, feedback interneuron; FF-IN, feedforward interneuron; SLK-KD, pyramidal neuron with reduced levels of SLK (knockdown). Red circle indicates the feedforward motif that is affected, while feedforward inhibition on other pyramidal cells is unaffected.

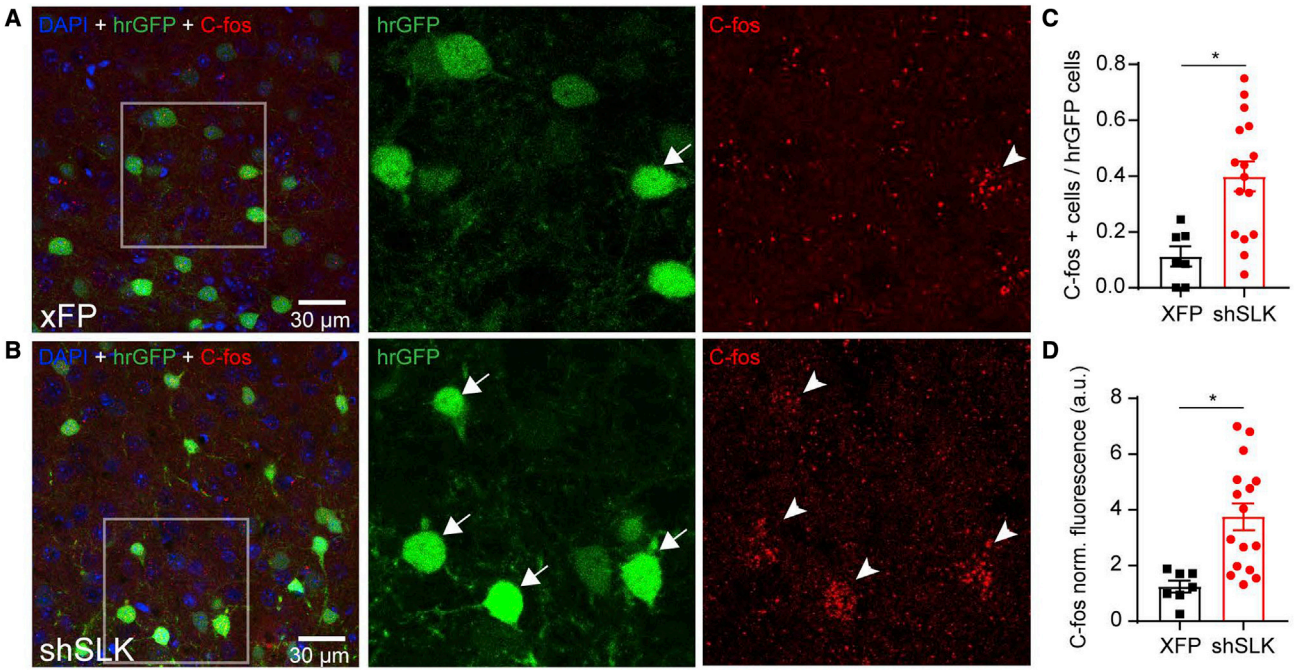


**Figure 5. shSLK neurons exhibit abnormal levels of basal activity**

(A and B) C-fos immunostaining of cortical slices electroporated with control XFP (A) and shSLK (B). XFP electroporated cells (arrow) showed sporadic expression of c-fos (arrowhead). In contrast, shSLK electroporated neurons (arrows) displayed a more prominent c-fos protein expression (arrowheads).

(C and D) Quantification of the number of hrGFP-expressing neurons also expressing c-fos (C), and the c-fos labeling intensity (D) in control XFP and shSLK electroporated neurons. Data points represent averages of all ROIs in individual animals (XFP = 7 and shSLK = 16 mice; quantification done in a total of 1,266 hrGFP-positive neurons). Asterisks indicate significance in unpaired t test ($p = 0.0028$ for (C), $p = 0.0031$ for (D), test performed considering N of mice as independent replicates). Data are represented as mean ± SEM.

Figure S8). No behavioral effects of focal SLK-KD could be observed in the open field, including locomotion speed, distance traveled, or time spent in the center of the arena (Figure S9; Table S6).

## Cell-autonomous regulation of inhibition ensures robust network dynamics

To evaluate the effect of cell-autonomous adjustment of inhibition on the network dynamics of PCs, we performed simulations of PC activity in response to biologically realistic synaptic input. This input was constrained based on an anatomically realistic network model of the rat barrel cortex (Figures 6A and 6B),[17,18] and with the activity of presynaptic neurons reflecting cell-type-specific spontaneous and sensory-evoked activity measured experimentally.[19] Similar to our previous simulations in layer IV[12] and layer V,[20] here we simulated the activity of all PCs in layer II/III of a single barrel column (n = 2,486), which received synaptic input mimicking spontaneous network activity and sensory-evoked activity in response to a sensory stimulus of the somatotopically aligned whisker (Figure 6C). Inhibition was either adjusted globally, i.e., the strength of all inhibitory synapses was scaled by the same amount, or cell autonomously, i.e., the strength of inhibitory synapses could be scaled by a different value for each PC. With the cell-autonomous adjustment, we find sparse activity that varies between trials (Figure 6D), with a narrow distribution of spike rates and few quiescent cells (Figure 6E), consistent with the sparse coding empirically observed in PCs. Conversely, with global adjustment, we find a broad distribution of spike rates, with more quiescent cells and many cells which spike persistently at very high rates (Figures 6D and 6E). We performed a sensitivity analysis to evaluate the effect of the fraction of inhibitory cells whose synaptic strengths are adjusted cell autonomously, from 0% to 100%. It has been reported that 40%–50% of INs are Pv expressing,[21] and indeed we find that even adjusting only 50% of inhibition substantially reduced the number of quiescent cells during both spontaneous and sensory-evoked network, simulations (Figure 6F). To elucidate the mechanism underlying these observations, we examined the relationship between inhibition and excitation during spontaneous activity. In accordance with our findings in SLK-deficient neurons (see Figure 2M), the lack of cell-autonomous adjustment of inhibition led to a loss of precise tuning of excitation-inhibition ratios across pyramidal neurons. Specifically, the ratio of excitation to inhibition received by PCs during spontaneous activity was more broadly distributed in the case of global versus cell-autonomous inhibitory adjustment (Figure 6G). Moreover, the more inhibition is adjusted cell autonomously, the lower the variability in excitation-inhibition ratio (Figure 6H). We therefore propose that cell-autonomous regulation of inhibition by PCs could constitute a developmental strategy to ensure robust network dynamics by minimizing excitation-inhibition imbalance.

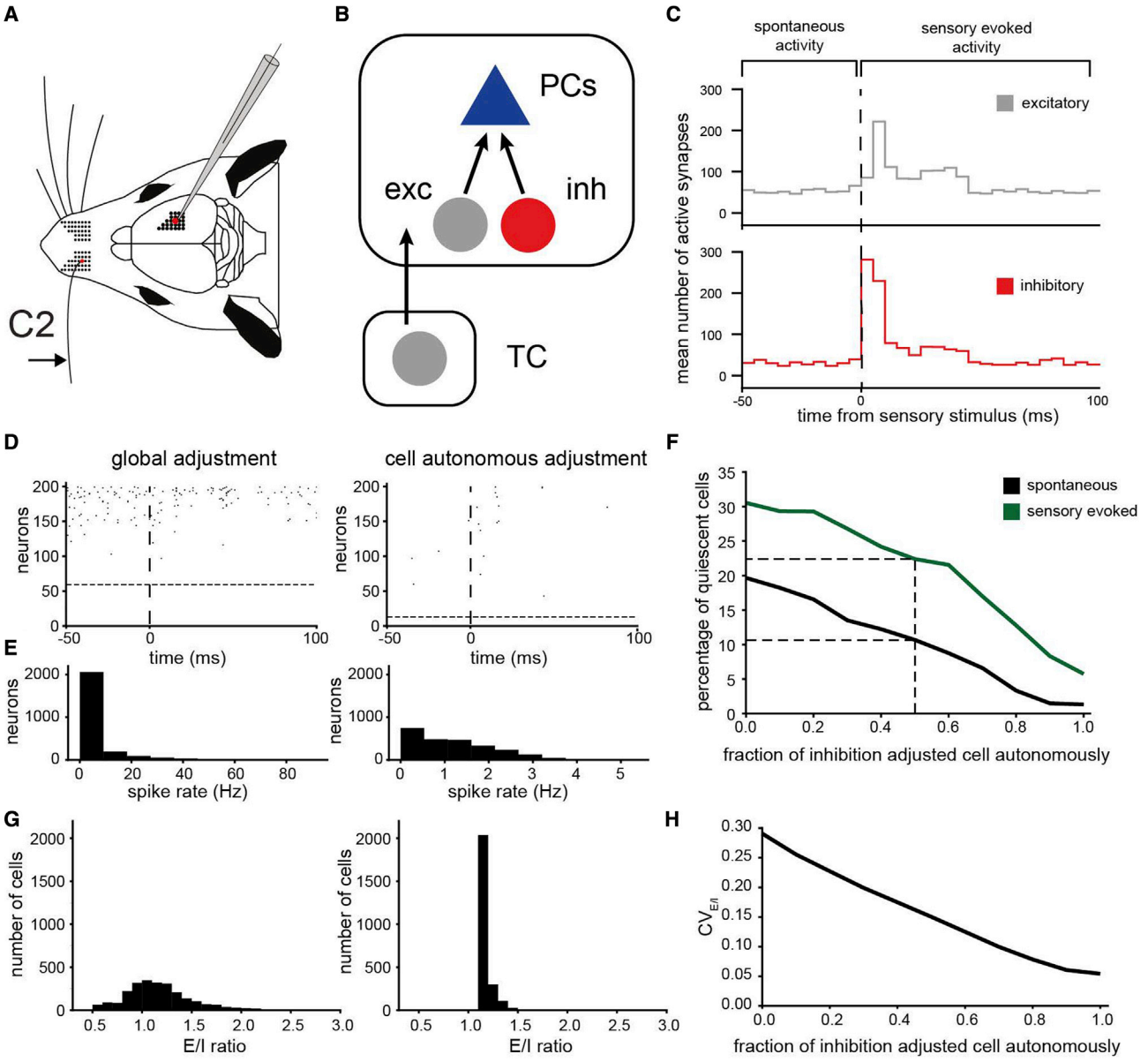


**Figure 6. Cell-autonomous regulation of inhibition ensures robust network dynamics**

(A) The C2 column of the rat vibrissal cortex (barrel cortex) and its somatotopically aligned whisker, which was deflected to provide a sensory stimulus.

(B) All PCs in layer II/III of the barrel column representing the C2 whisker (n = 2,486) were simulated. They received synaptic input from all intracortical excitatory and inhibitory cell types, as well as thalamocortical input from the primary thalamus of the whisker system—the ventral posterior medial nucleus.

(C) Average synaptic input received by a PC in the C2 column during spontaneous network activity and during simulation of a sensory stimulus (i.e., passive deflection of the C2 whisker (de Kock et al.).[19]

(D) Single-trial raster plots for 200 randomly selected cells following a sensory stimulus at t = 0, sorted by mean evoked response over 100 trials. Cells below the horizontal dashed line were quiescent (no evoked response in 100 trials). The strength of inhibitory synapses was adjusted either globally, or cell autonomously for 100% of inhibitory cells.

(E) Spontaneous spike rates measured over 60 s.

(F) Percentage of quiescent cells during spontaneous and sensory-evoked activity for simulations with different fractions of inhibition adjusted cell-autonomously.

(G) Mean ratio of excitation to inhibition during 60 s of spontaneous activity.

(H) Coefficient of variation of the E/I ratio for simulations with different fractions of inhibition adjusted cell-autonomously.

## Activity-dependent regulation of SLK

So far, the results suggest that SLK may be important to cell autonomously adjust inhibition to the levels of excitation cortical neurons receive. This would require that SLK activity itself can be regulated by neuronal activity. Because SLK activity is known to be strongly regulated by phosphorylation, we asked if SLK

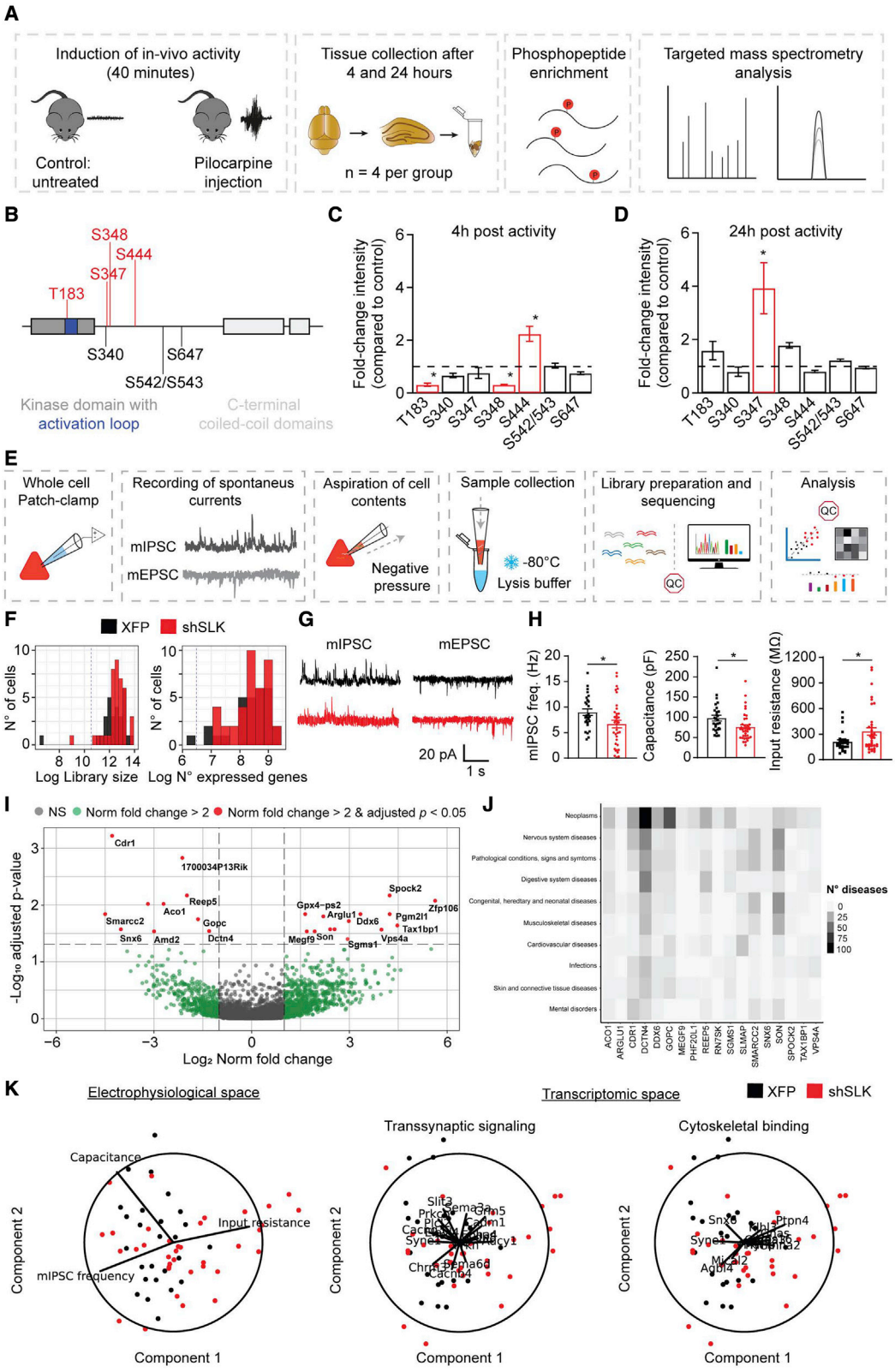


*(legend on next page)*

phosphorylation status changes in response to an episode of chemically induced synchronous activity. SLK phosphorylation sites and the SLK protein levels were monitored 4 and 24 h after terminating neuronal activity (Figure 7A). Using targeted mass spectrometry analysis of hippocampal tissue, quantitative data were obtained for six localized phosphorylation sites (T183, S340, S347, S348, S444, and S647) and one ambiguous site location (S542/S543) (Figure 7B). At 4 h, the phosphorylation of T183 and S348 was decreased and the phosphorylation of S444 was increased. At 24 h, S347 phosphorylation was increased, and all other sites had no significant changes (Figures 7C and 7D). The underlying level of SLK protein did not change at 4 or 24 h (data not shown). T183 is an activation segment autophosphorylation site that increases SLK activity.[22,23] S347 and S348 phosphorylation inhibits SLK activity.[24] S444 phosphorylation has no known function. These results show that activity leads to temporally regulated phosphorylation at multiple sites, implying a complex activity-dependent regulation of SLK.

### Identification of candidate molecular pathways correlated with altered inhibitory function in cortical pyramidal neurons using patch-seq

The importance of SLK in cell-autonomous regulation of feedforward Pv-mediated inhibition raises the question of what molecular, neuron-intrinsic pathways might be involved in the regulation of inhibition. To assess the relationship between the excitatory-inhibitory balance, and the transcriptional landscape, we established patch-seq protocols, with which electrophysiological properties can be correlated with gene expression patterns (Figure 7E). The patch-seq technique combines whole-cell patch-clamping and single-cell RNA sequencing (scRNA-seq). In brief, cortical layer II/III neurons either expressing control XFP or shSLK were recorded with a patch-clamp electrode containing internal solution optimized for patch-seq (Figure 7E). Following the electrophysiological recordings, the cell contents were aspirated into the patch pipette and extruded into a tube containing lysis buffer for cDNA synthesis. We recorded from 91 hrGFP expressing neurons, of which 66 cells were suitable for combined functional and scRNA-seq analysis following rigorous quality control checks after library preparation and alignment of reads (38 shSLK and 28 XFP neurons, Figure 7F; see STAR Methods).

The functional analyses confirmed the selective reduction of inhibition in SLK KD neurons, with a reduction of mIPSC frequencies but unchanged mEPSC frequencies (Figures 7G and 7H). Moreover, we also identified a reduction in cell capacitance and an increase in input resistance in this set of recordings (Figure 7H; Table S1 for additional mPSC and passive membrane properties). We then determined which genes were differentially expressed when comparing shSLK and XFP neurons. Using a recently described analysis approach that has been shown to be particularly suitable for scRNA-seq data with a high number of zero counts (DEsingle, Miao et al.[25]), we found 24 differentially expressed (DE) genes (false discovery rate adjusted $p < 0.05$). Ten genes were downregulated in shSLK neurons, and 14 genes displayed upregulation (Figure 7I; gene list in Table S2). For the 24 DE genes, we explored the association with human diseases using the Disgenet2r platform, which includes gene-disease associations from a large number of databases. Eighteen of the genes found to be altered in SLK-deficient neurons have been described to be involved in human disorders, especially in neoplasms and nervous system pathologies (Figure 7J), consistent with the role of SLK in cortical malformations and ganglioglioma.[14]

To determine how the transcriptomic profile of shSLK neurons relates to the changes in electrophysiological parameters, we applied a sparse reduced-rank regression (RRR) approach to predict the three electrophysiological properties we found to be altered in shSLK neurons. This approach uses a low-dimensional representation of the expression of selected genes,[26] and allows to visualize relationships between

**Figure 7. Activity-modified phosphorylation of SLK and correlation of altered inhibitory function of shSLK neurons with candidate molecular pathways using patch-seq**

(A) Workflow schematic of quantitative targeted mass spectrometry analysis.

(B) Localization of the seven phosphorylation sites that were quantified.

(C and D) Fold change in phosphorylation 4 h (C) and 24 h (D) after *in vivo* activity.

(E) Workflow schematic of patch-seq methodology. Cortical layer II/III neurons either expressing control XFP or shSLK were recorded with a patch-clamp electrode containing internal solution optimized for patch-seq. Next, cell contents were aspirated into the patch pipette, extruded into a tube containing an optimized lysis buffer, and stored at −80°C. Quality control checks were performed on cDNA library profiles and aligned reads to discard low-quality samples.

(F) Histograms of log-transformed total number of reads (left) and number of detected genes (right) for all cells in the dataset. Samples with values lower than 3 times the mean absolute deviation (MAD) (dashed lines) were classified as low quality and removed from further analysis.

(G) Representative examples of miniature IPSCs (mIPSCs) in electroporated XFP (black traces) and shSLK neurons (red traces).

(H) IPSC frequency (left), cell capacitance (middle), and input resistance (right) comparisons of neurons expressing shSLK and control XFP. Asterisks indicate significance in unpaired t test ($p = 0.0289$ for IPSC frequency, $p = 0.0.155$ for cell capacitance).

(I) Volcano plot showing 24 differentially expressed genes (DE) (red circles). Dashed lines demark genes with an absolute normalized fold change higher than 2 (vertical dashed lines) and a false discovery rate adjusted p value lower than 0.05 (horizontal dashed line).

(J) Heatmap displaying the total number of diseases grouped by disease class that are associated with DE genes according to the gene discovery platform Disgenet2r. The plot shows the 10 disease classes with the highest number of diseases associated with DE genes.

(K) Sparse reduced-rank regression model to visualize relationships between electrophysiological features and gene expression. Electrophysiological data were linearly projected to a low-dimensional space (left plot). The model selected 113 genes that allowed the visual reconstruction of electrophysiological data. The two components of the rank-2 model are shown. For visualization purposes, the transcriptomic space was plotted labeling different relevant gene ontology terms separately (middle panel, transsynaptic signaling; right panel, cytoskeletal binding). Lines represent correlations of the electrophysiological and transcriptomic variables with both components, with longer lines indicating stronger correlations. The circle is set to represent a correlation of 1. Similar directions of the variables can suggest an association between electrophysiological features and the expression of genes. Data in bar plots are represented as mean ± SEM.

electrophysiological features and gene expression. We used cross-validation to tune the hyperparameters (Figures S10A–S10C) and obtained a model that selected 113 candidate genes best explaining the variability of the electrophysiological data (Table S3). Ontology analyses incorporating the entire mouse genome revealed enrichment of gene terms relevant to neuron morphology and physiology (Tables S4 and S5). We then projected the gene expression and electrophysiological properties of our samples onto the first two dimensions (Figure 7K). Lines represent the correlation of the variables with both components, with a maximum correlation of 1 being indicated by the circle. Similar directions of the electrophysiological and transcriptomic variables suggest an association between functional features and the expression of genes. The visual representation in the reduced electrophysiological space shows how shSLK and XFP neurons tend to be separated from each other in the first two components (Figure 7K, left panel). For visualization, we plotted genes selected by RRR and corresponding to specific gene ontology terms within the transcriptomic space. Interestingly, a number of genes related to transsynaptic signaling were prominently selected by our model and aligned to the electrophysiological variables in the reduced space, suggesting an association between the functional consequences of the loss of SLK and changes in transsynaptic communication[26] (Figure 7K, middle panel). Moreover, genes encoding for cytoskeletal interacting proteins were selected by the model and aligned to the functional properties (Figure 7K, right panel), consistent with the known function of SLK in cytoskeletal dynamics. Ion channels and neurodevelopmental-related genes were two further prominent gene categories within the gene population selected by the model (Figure S10D).

Snx6, a member of the sorting nexin family involved in intracellular trafficking and axon guidance,[27] was differentially regulated in our DE analysis (~18-fold downregulation, Figure 7I) and was also selected by the sparse RRR model (Figure 7K). We therefore performed immunohistochemistry to elucidate if SNX6 is regulated at the protein level. Immunostaining of cortical slices electroporated with control XFP or shSLK revealed that shSLK electroporated neurons expressed lower levels of Snx6 protein (Figures S11A–S11C).

Collectively, these results suggest that the inhibitory and other membrane alterations observed in pyramidal neurons after SLK loss may be related to changes in the expression of specific gene families known to be relevant for neuronal transsynaptic signaling and cytoskeletal dynamics.

## DISCUSSION

In this study, we describe a mechanism dependent on SLK that allows pyramidal neurons to cell autonomously regulate the amount of inhibition they receive from Pv-expressing INs.

### Cell-autonomous effects versus global regulation of inhibition

In general terms, cell-autonomous regulation of inhibition is thought to be required to adjust it to the large differences in excitatory thalamocortical inputs that exist from cell to cell.[9,12] The SLK-dependent mechanism described here allows such a cell-intrinsic regulation (illustrated in Figure 4M), based on cell-specific regulation of Pv-IN-mediated inputs. This is consistent with a study showing that regulation of inhibitory synapses originating from Pv-containing INs is important to maintaining excitation-inhibition balance across individual cortical neurons.[11]

This cell-autonomous regulatory mechanism contrasts with other, known mechanisms that act across multiple cells or entire brain regions. For instance, different mechanisms that regulate recruitment of INs have been described. Excitatory recruitment of SST-expressing INs is regulated by an Elfn1-dependent pathway.[28] Likewise, non-Hebbian synaptic plasticity selectively affecting the recruitment of SST-containing INs in this pathway has been described.[29] The neuregulin1-ErbB4 signaling cascade, on the other hand, selectively regulates the formation of inhibitory synapses from Pv-expressing INs onto pyramidal neurons, as well as the formation of excitatory synapses onto Pv-INs,[30,31] and therefore powerfully affects the excitability of the Pv-IN system.[32] However, these types of regulation typically affect the efficacy of large IN populations. Therefore, it has been argued that these mechanisms cannot underlie cell-specific regulation of inhibition, because these IN populations contact PCs in a widespread and largely indiscriminate fashion.[33,34]

Our results from an anatomically[17,18] and functionally well-constrained model[12,17,20] show that cell-autonomous adjustment of inhibition is critical for proper cortical function, and is essential to maintain constant excitation-inhibition ratios across different PCs. Importantly, we found that mimicking sensory stimulation-evoked inputs caused activity similar to empirically observed spiking only when cell-autonomous adjustment of inhibition is implemented, even if cell-autonomous regulation applies only to a fraction (50%) of inhibitory inputs. Moreover, we found that lack of cell-autonomous regulation of inhibition causes a large fraction of silent pyramidal neurons that cannot respond to sensory stimuli, while the remaining neurons respond with very high firing rates, indicating the loss of their ability to code information sparsely. Therefore, the increase of c-fos levels after SLK loss is consistent with a subpopulation of cortical neurons with high spike rates caused by impaired intrinsic adjustment of inhibition. Thus, cell-autonomous regulation is an essential mechanism to ensure that cortical pyramidal neurons can participate efficiently and robustly in cortical information coding.

The participation of SLK in such a regulation process implies that SLK itself can be regulated by activity, such that abnormal I/E balance leads to increased activity, and subsequently to the regulation of SLK. We have shown that activity leads to a complex, temporally regulated pattern of phosphorylation of SLK at multiple sites, indicating an intricate regulation of SLK by activity. SLK protein levels displayed no activity-dependent changes, suggesting that activity is linked to SLK activity via phospho-signaling and not protein expression. Interestingly, we observed a decrease of S348 phosphorylation at early time points, while at 24 h the phosphorylation at the adjacent S347 site was increased. S347/S348 phosphorylation is inhibitory for SLK activity via a casein kinase 2 mechanism (Chaar et al.,[24] 16,837,460). This may suggest a biphasic regulation, with a time window for homeostatic regulation of inhibition by activity. However, further work will be required to elucidate how the

different phosphorylation sites interact to resolve the cell-type-specific phosphorylation pattern of SLK, and disentangle the contribution of other factors, such as protein homodimerization, protein-protein interactions, and subcellular localization.[22,23,35–38]

### Preferential effects of SLK on feedforward inhibition

The cell-autonomous regulation of inhibition did not impact all inhibitory synapses indiscriminately. Instead, it affected mainly synapses originating from Pv-INs. It is well-established that Pv-expressing INs strongly contribute to cortical feedforward inhibition because feedforward thalamic inputs strongly activate these INs.[5–7] Conversely, SST-expressing INs are weakly recruited by thalamic inputs but are strongly activated by intracortical recurrent axon collaterals, thus contributing preferentially to feedback inhibition.[7] Thus, the selective effects of SLK on Pv-mediated inhibition are consistent with the preferential effects on feedforward inhibition.

The relatively selective effects of SLK on feedforward inhibition are interesting in themselves. Feedforward and feedback circuits are thought to serve different computational roles. In general, feedforward inhibition is thought to perform input normalization, which is important for the capability of pyramidal neurons to respond in a graded fashion to a large range of input strengths.[1,39,40] In addition, feedforward inhibitory circuits are important in sharpening the temporal resolution of thalamically driven action potentials.[41] These computational mechanisms are distinct from those served by feedback inhibition and suggest more specific roles for SLK-mediated regulation of inhibition.

### Cellular mechanisms of cell-autonomous regulation

We have searched for possible candidate pathways underlying cell-autonomous regulation of inhibition using patchSeq approaches, which allow correlation of transcriptional changes with functional changes in GABAergic inhibition. DE analysis revealed 10 down- and 14 upregulated genes in shSLK neurons compared with the control group. Gene-disease associations showed that 16 of these DE genes have been linked to human diseases, especially neoplasms and nervous system disorders. Interestingly, many of these neurological diseases are related to cognitive disabilities and epilepsy, in which impaired Pv-IN-mediated inhibition is a prominent pathophysiological feature.[42–48] In addition, the gene pattern in SLK-deficient neurons shows an association with neoplasms and CNS disorders (see Figure 7F). Indeed, SLK was found to be strongly reduced in neurons as pathognomonic cell type of a large spectrum of brain malformations, including cortical dysplasias and gangliogliomas.[14] Interestingly, both of these disorders are commonly associated with hyperexcitability and seizures, in keeping with the role of SLK in adjusting feedforward inhibition described here.

That a postsynaptic modification in layer II/III pyramidal neurons (SLK deficiency) leads to loss of specific GABAergic synaptic sites defined by their presynaptic identity suggests a transsynaptic mechanism (see Figure 4M, left panel, red circle). In addition, the sparse RRR analysis revealed that the expression of genes related to transsynaptic communication and cytoskeletal dynamics are related to the changes in the functional properties after SLK loss. We therefore particularly considered candidate genes connected to transsynaptic regulation of inhibition. SNX6 expression was significantly downregulated by SLK knockdown, a finding confirmed by immunohistochemistry. SNX6 encodes a member of the sorting nexin family, which is involved in intracellular trafficking and axon guidance.[27] Interestingly, SNX6 was proposed to interact with the semaphorin pathway,[27] a molecular cascade that can trans-synaptically regulate inhibitory synapse development.[49] Further studies suggest a cascade where SNX6 may interact with SNX27 through its PDZ domain, regulating neuroligin-2 surface levels and thereby GABAergic transmission.[50–52] This is particularly interesting since loss of neuroligin-2 produces similarly selective functional consequences to the loss of SLK. In the somatosensory cortex, genetic deletion of neuroligin-2 decreased the amplitude of IPSCs originating from Pv- but not from SST-expressing INs.[53] As a consequence, excitatory cells but not Pv- or SST-positive INs display overexcitation in the amygdala after anxiogenic stimuli.[54]

In summary, our data indicate that SLK participates in the cell-autonomous regulation of circuit-specific inhibition, which is critical to maintaining an appropriate balance between excitation and inhibition. Such a mechanism is important to ensure the robust and sparse coding features empirically observed in cortical PCs.

### Limitations of the study

Collectively, our results suggest that activity can modulate SLK, and that this molecule is important in cell-autonomous regulation of inhibition. We note that, although our phosphoproteomic data clearly show complex regulation of SLK phosphorylation by neuronal activity, in a manner predicting that SLK activity changes, it will be necessary to more precisely understand the link between neuronal activity and SLK activity. We have identified a number of molecules as potential downstream targets of SLK signaling, including SNX6. We note that these are candidate genes, and further work will be required to dissect which of the potential downstream signaling molecules is most important in regulating excitation-inhibition balance.

## STAR★METHODS

Detailed methods are provided in the online version of this paper and include the following:

- KEY RESOURCES TABLE
- RESOURCE AVAILABILITY
  - Lead contact
  - Materials availability
  - Data and code availability
- EXPERIMENTAL MODEL AND SUBJECT DETAILS
- METHOD DETAILS
  - Animals
  - Generation of constructs
  - Intraventricular in utero electroporation
  - Stereotaxic viral gene transfer
  - Slice preparation

- Electrophysiological recordings
- Electric and optogenetic stimulation
- Patch-clamp recording analysis
- Immunohistochemistry
- Patch-clamp recordings and RNA collection
- Library preparation, sequencing, and gene alignment
- Patch-seq analysis
- Induction of status epilepticus and extraction of hippocampal tissue for targeted mass spectrometry
- Targeted mass spectrometry analysis of SLK phosphorylation and protein levels
- Computational modeling
- Open field behavior

● QUANTIFICATION AND STATISTICAL ANALYSIS

## SUPPLEMENTAL INFORMATION

Supplemental information can be found online at https://doi.org/10.1016/j.celrep.2022.111757.

## ACKNOWLEDGMENTS

We are very grateful to Lea Keller and T.O. for technical support and help with breeding and genotyping. We acknowledge the support of the Imaging Core Facility and the Viral Core Facility of the Bonn Technology Campus Life Sciences (DFG Project nos. 266686698, 388169927, and 388168919). We acknowledge the support of the Children's Medical Research Institute Biomedical Proteomics Facility. The work was supported by the SFB 1089, Project A06 to S.S. and H.B., Project C05 to M.O., and EXC 2151 under the Federal Excellence Strategy of the Deutsche Forschungsgemeinschaft (DFG, German Research Foundation) to H.B. and J.S., the intramural support program BONFOR to S.S., A.B., and H.B., and the European Research Council under the European Union's Horizon 2020 research and innovation program (grant agreement 633428) to M.O. P.R., A.Q., R.F., and A. Bast were supported by the IMPRS Brain and Behavior.

## AUTHOR CONTRIBUTIONS

H.B., P.R., S.S., and A. Becker conceived and planned the study. P.R. performed all electrophysiological experiments and data analysis, as well as immunostaining experiments and patchSeq experiments. A.Q. performed *in utero* electroporations and generated the required plasmids. P.R., together with the PRECISE group (J.L.S., T.U., and K.H.), established patchSeq and did sequencing and data analysis. R.F., A. Bast, and M.O. performed computational modeling. M.H.S. performed the mass spectrometry experiments. M.E.G. analyzed the mass spectrometry data. H.B. and P.R. wrote the manuscript. All authors participated in the interpretation of data and preparation of the manuscript.

## DECLARATION OF INTERESTS

The authors declare no competing interests.

Received: March 24, 2022
Revised: October 18, 2022
Accepted: November 9, 2022
Published: December 6, 2022

## REFERENCES

1. Isaacson, J.S., and Scanziani, M. (2011). How inhibition shapes cortical activity. Neuron *72*, 231–243.
2. Douglas, R.J., and Martin, K.A.C. (2004). Neuronal circuits of the neocortex. Annu. Rev. Neurosci. *27*, 419–451.
3. Douglas, R.J., and Martin, K.A. (2007). Mapping the matrix. The ways of neocortex. Neuron *56*, 226–238.
4. Constantinople, C.M., and Bruno, R.M. (2013). Deep cortical layers are activated directly by thalamus. Science *340*, 1591–1594.
5. Beierlein, M., Gibson, J.R., and Connors, B.W. (2003). Two dynamically distinct inhibitory networks in layer 4 of the neocortex. J. Neurophysiol. *90*, 2987–3000.
6. Cruikshank, S.J., Lewis, T.J., and Connors, B.W. (2007). Synaptic basis for intense thalamocortical activation of feedforward inhibitory cells in neocortex. Nat. Neurosci. *10*, 462–468.
7. Sermet, B.S., Truschow, P., Feyerabend, M., Mayrhofer, J.M., Oram, T.B., Yizhar, O., Staiger, J.F., and Petersen, C.C. (2019). Pathway-, layer- and cell-type-specific thalamic input to mouse barrel cortex. Elife *8*, e52665.
8. Okun, M., Steinmetz, N., Cossell, L., Iacaruso, M.F., Ko, H., Barthó, P., Moore, T., Hofer, S.B., Mrsic-Flogel, T.D., Carandini, M., et al. (2015). Diverse coupling of neurons to populations in sensory cortex. Nature *521*, 511–515.
9. Cohen-Kashi Malina, K., Mohar, B., Rappaport, A.N., and Lampl, I. (2016). Local and thalamic origins of correlated ongoing and sensory-evoked cortical activities. Nat. Commun. *7*, 12740.
10. Okun, M., and Lampl, I. (2008). Instantaneous correlation of excitation and inhibition during ongoing and sensory-evoked activities. Nat. Neurosci. *11*, 535–537.
11. Xue, M., Atallah, B.V., and Scanziani, M. (2014). Equalizing excitation-inhibition ratios across visual cortical neurons. Nature *511*, 596–600.
12. Landau, I.D., Egger, R., Dercksen, V.J., Oberlaender, M., and Sompolinsky, H. (2016). The impact of structural heterogeneity on excitation-inhibition balance in cortical networks. Neuron *92*, 1106–1121.
13. Garland, B., Delisle, S., Al-Zahrani, K.N., Pryce, B.R., and Sabourin, L.A. (2021). The Ste20-like kinase - a Jack of all trades? J. Cell Sci. *134*, jcs258269.
14. Schoch, S., Quatraccioni, A., Robens, B.K., Maresch, R., van Loo, K.M.J., Cases-Cunillera, S., Kelly, T., Opitz, T., Borger, V., Dietrich, D., et al. (2021). Ste20-like kinase is critical for inhibitory synapse maintenance and its deficiency confers a developmental dendritopathy. J. Neurosci. *41*, 8111–8125.
15. Oberlaender, M., Ramirez, A., and Bruno, R.M. (2012). Sensory experience restructures thalamocortical axons during adulthood. Neuron *74*, 648–655.
16. Wimmer, V.C., Bruno, R.M., Kock, C.P.J. de, Kuner, T., and Sakmann, B. (2010). Dimensions of a projection column and architecture of VPM and POm axons in rat vibrissal cortex. Cereb Cortex *20*, 2265–2276.
17. Egger, R., Dercksen, V.J., Udvary, D., Hege, H.-C., and Oberlaender, M. (2014). Generation of dense statistical connectomes from sparse morphological data. Front. Neuroanat. *8*, 129.
18. Udvary, D., Harth, P., Macke, J.H., Hege, H.-C., Kock, C.P. de, Sakmann, B., and Oberlaender, M. (2020). The Impact of Neuron Morphology on Cortical Network Architecture.
19. Kock, C.P.J. de, Bruno, R.M., Spors, H., and Sakmann, B. (2007). Layer- and cell-type-specific suprathreshold stimulus representation in rat primary somatosensory cortex. J. Physiol *581*, 139–154.
20. Egger, R., Narayanan, R.T., Guest, J.M., Bast, A., Udvary, D., Messore, L.F., Das, S., Kock, C.P.J. de, and Oberlaender, M. (2020). Cortical output is gated by horizontally projecting neurons in the deep layers. Neuron *105*, 122–137.e8.
21. Perumal, M.B., and Sah, P. (2021). Inhibitory circuits in the basolateral amygdala in Aversive learning and memory. Front. Neural Circ. *15*, 633235.
22. Luhovy, A.Y., Jaberi, A., Papillon, J., Guillemette, J., and Cybulsky, A.V. (2012). Regulation of the Ste20-like kinase, SLK: involvement of activation segment phosphorylation. J. Biol. Chem. *287*, 5446–5458.

23. Cybulsky, A.V., Guillemette, J., Papillon, J., and Abouelazm, N.T. (2017). Regulation of Ste20-like kinase, SLK, activity: dimerization and activation segment phosphorylation. PLoS One *12*, e0177226.

24. Chaar, Z., O'Reilly, P., Gelman, I., and Sabourin, L.A. (2006). v-Src-dependent down-regulation of the Ste20-like kinase SLK by casein kinase II. J. Biol. Chem. *281*, 28193–28199.

25. Miao, Z., Deng, K., Wang, X., and Zhang, X. (2018). DEsingle for detecting three types of differential expression in single-cell RNA-seq data. Bioinformatics *34*, 3223–3224.

26. Kobak, D., Bernaerts, Y., Weis, M.A., Scala, F., Tolias, A.S., and Berens, P. (2021). Sparse reduced-rank regression for exploratory visualisation of paired multivariate data. Royal Stata Society Series C *70*, 980–1000.

27. Simonetti, B., Paul, B., Chaudhari, K., Weeratunga, S., Steinberg, F., Gorla, M., Heesom, K.J., Bashaw, G.J., Collins, B.M., and Cullen, P.J. (2019). Molecular identification of a BAR domain-containing coat complex for endosomal recycling of transmembrane proteins. Nat. Cell Biol. *21*, 1219–1233.

28. Sylwestrak, E.L., and Ghosh, A. (2012). Elfn1 regulates target-specific release probability at CA1-interneuron synapses. Science *338*, 536–540.

29. Lamsa, K.P., Heeroma, J.H., Somogyi, P., Rusakov, D.A., and Kullmann, D.M. (2007). Anti-Hebbian long-term potentiation in the hippocampal feedback inhibitory circuit. Science *315*, 1262–1266.

30. Fazzari, P., Paternain, A.V., Valiente, M., Pla, R., Luján, R., Lloyd, K., Lerma, J., Marín, O., and Rico, B. (2010). Control of cortical GABA circuitry development by Nrg1 and ErbB4 signalling. Nature *464*, 1376–1380.

31. Ting, A.K., Chen, Y., Wen, L., Yin, D.-M., Shen, C., Tao, Y., Liu, X., Xiong, W.-C., and Mei, L. (2011). Neuregulin 1 promotes excitatory synapse development and function in GABAergic interneurons. J. Neurosci. *31*, 15–25.

32. Sun, Y., Ikrar, T., Davis, M.F., Gong, N., Zheng, X., Luo, Z.D., Lai, C., Mei, L., Holmes, T.C., Gandhi, S.P., et al. (2016). Neuregulin-1/ErbB4 signaling regulates visual cortical plasticity. Neuron *92*, 160–173.

33. Fino, E., and Yuste, R. (2011). Dense inhibitory connectivity in neocortex. Neuron *69*, 1188–1203.

34. Packer, A.M., and Yuste, R. (2011). Dense, unspecific connectivity of neocortical parvalbumin-positive interneurons. A canonical microcircuit for inhibition? J. Neurosci. *31*, 13260–13271.

35. Cybulsky, A.V., Takano, T., Papillon, J., Hao, W., Mancini, A., Di Battista, J.A., and Cybulsky, M.I. (2007). The 3'-untranslated region of the Ste20-like kinase SLK regulates SLK expression. Am. J. Physiol. Ren. Physiol. *292*, F845–F852.

36. Storbeck, C.J., Wagner, S., O'Reilly, P., Mckay, M., Parks, R.J., Westphal, H., and Sabourin, L.A. (2009). The Ldb1 and Ldb2 transcriptional cofactors interact with the Ste20-like kinase SLK and regulate cell migration. Mol. Biol. Cell *20*, 4174–4182.

37. Delarosa, S., Guillemette, J., Papillon, J., Han, Y.-S., Kristof, A.S., and Cybulsky, A.V. (2011). Activity of the Ste20-like kinase, SLK, is enhanced by homodimerization. Am. J. Physiol. Ren. Physiol. *301*, F554–F564.

38. Jaberi, A., Hooker, E., Guillemette, J., Papillon, J., Kristof, A.S., and Cybulsky, A.V. (2015). Identification of Tpr and $\alpha$-actinin-4 as two novel SLK-interacting proteins. Biochim. Biophys. Acta *1853*, 2539–2552.

39. Pouille, F., Marin-Burgin, A., Adesnik, H., Atallah, B.V., and Scanziani, M. (2009). Input normalization by global feedforward inhibition expands cortical dynamic range. Nat. Neurosci. *12*, 1577–1585.

40. Braganza, O., and Beck, H. (2018). The circuit motif as a conceptual tool for multilevel neuroscience. Trends Neurosci. *41*, 128–136.

41. Gabernet, L., Jadhav, S.P., Feldman, D.E., Carandini, M., and Scanziani, M. (2005). Somatosensory integration controlled by dynamic thalamocortical feed-forward inhibition. Neuron *48*, 315–327.

42. Yu, F.H., Mantegazza, M., Westenbroek, R.E., Robbins, C.A., Kalume, F., Burton, K.A., Spain, W.J., McKnight, G.S., Scheuer, T., and Catterall, W.A. (2007). Reduced sodium current in GABAergic interneurons in a mouse model of severe myoclonic epilepsy in infancy. Nat. Neurosci. *10*, 134.

43. Verret, L., Mann, E.O., Hang, G.B., Barth, A.M., Cobos, I., Ho, K., Devidze, N., Masliah, E., Kreitzer, A.C., Mody, I., et al. (2012). Inhibitory interneuron deficit links altered network activity and cognitive dysfunction in Alzheimer model. Cell *149*, 708–721.

44. Iaccarino, H.F., Singer, A.C., Martorell, A.J., Rudenko, A., Gao, F., Gillingham, T.Z., Mathys, H., Seo, J., Kritskiy, O., Abdurrob, F., et al. (2016). Gamma frequency entrainment attenuates amyloid load and modifies microglia. Nature *540*, 230–235.

45. Selimbeyoglu, A., Kim, C.K., Inoue, M., Lee, S.Y., Hong, A.S.O., Kauvar, I., Ramakrishnan, C., Fenno, L.E., Davidson, T.J., Wright, M., et al. (2017). Modulation of prefrontal cortex excitation/inhibition balance rescues social behavior in CNTNAP2-deficient mice. Sci. Transl. Med. *9*, eaah6733.

46. Vogt, D., Cho, K.K.A., Shelton, S.M., Paul, A., Huang, Z.J., Sohal, V.S., and Rubenstein, J.L.R. (2018). Mouse Cntnap2 and human CNTNAP2 ASD Alleles cell autonomously regulate PV+ cortical interneurons. Cereb Cortex *28*, 3868–3879.

47. Hijazi, S., Heistek, T.S., Scheltens, P., Neumann, U., Shimshek, D.R., Mansvelder, H.D., Smit, A.B., and van Kesteren, R.E. (2020). Early restoration of parvalbumin interneuron activity prevents memory loss and network hyperexcitability in a mouse model of Alzheimer's disease. Mol. Psychiatry *25*, 3380–3398.

48. Amegandjin, C.A., Choudhury, M., Jadhav, V., Carriço, J.N., Quintal, A., Berryer, M., Snapyan, M., Chattopadhyaya, B., Saghatelyan, A., and Di Cristo, G. (2021). Sensitive period for rescuing parvalbumin interneurons connectivity and social behavior deficits caused by TSC1 loss. Nat. Commun. *12*, 3653.

49. Frias, C.P., Liang, J., Bresser, T., Scheefhals, L., van Kesteren, M., van Dorland, R., Hu, H.Y., Bodzeta, A., van Bergen En Henegouwen, P.M.P., Hoogenraad, C.C., et al. (2019). Semaphorin4D induces inhibitory synapse formation by rapid stabilization of presynaptic boutons via MET coactivation. J. Neurosci. *39*, 4221–4237.

50. Binda, C.S., Nakamura, Y., Henley, J.M., and Wilkinson, K.A. (2019). Sorting nexin 27 rescues neuroligin 2 from lysosomal degradation to control inhibitory synapse number. Biochem. J. *476*, 293–306.

51. Halff, E.F., Szulc, B.R., Lesept, F., and Kittler, J.T. (2019). SNX27-Mediated recycling of neuroligin-2 regulates inhibitory signaling. Cell Rep. *29*, 2599–2607.e6.

52. Yong, X., Zhao, L., Deng, W., Sun, H., Zhou, X., Mao, L., Hu, W., Shen, X., Sun, Q., Billadeau, D.D., et al. (2020). Mechanism of cargo recognition by retromer-linked SNX-BAR proteins. PLoS Biol. *18*, e3000631.

53. Gibson, J.R., Huber, K.M., and Südhof, T.C. (2009). Neuroligin-2 deletion selectively decreases inhibitory synaptic transmission originating from fast-spiking but not from somatostatin-positive interneurons. J. Neurosci. *29*, 13883–13897.

54. Babaev, O., Botta, P., Meyer, E., Müller, C., Ehrenreich, H., Brose, N., Lüthi, A., and Krueger-Burg, D. (2016). Neuroligin 2 deletion alters inhibitory synapse function and anxiety-associated neuronal activation in the amygdala. Neuropharmacology *100*, 56–65.

55. Wang, T., Li, B., Nelson, C.E., and Nabavi, S. (2019). Comparative analysis of differential gene expression analysis tools for single-cell RNA sequencing data. BMC Bioinf. *20*, 40.

56. Piñero, J., Bravo, À., Queralt-Rosinach, N., Gutiérrez-Sacristán, A., Deu-Pons, J., Centeno, E., García-García, J., Sanz, F., and Furlong, L.I. (2017). DisGeNET: a comprehensive platform integrating information on human disease-associated genes and variants. Nucleic Acids Res. *45*, D833–D839.

57. Olson, A., Sheth, N., Lee, J.S., Hannon, G., and Sachidanandam, R. (2006). RNAi Codex: a portal/database for short-hairpin RNA (shRNA) gene-silencing constructs. Nucleic Acids Res. *34*, D153–D157.

58. Szczurkowska, J., Cwetsch, A.W., dal, M.M., Ghezzi, D., Ratto, G.M., and Cancedda, L. (2016). Targeted in vivo genetic manipulation of the mouse or rat brain by in utero electroporation with a triple-electrode probe. Nat. Protoc. *11*, 399–412.

59. Müller-Komorowska, D., Opitz, T., Elzoheiry, S., Schweizer, M., Ambrad Giovannetti, E., and Beck, H. (2020). Nonspecific expression in limited excitatory cell populations in interneuron-targeting cre-driver lines can have large functional effects. Front. Neural Circ. *14*, 16.

60. Liu, L., Ito, W., and Morozov, A. (2018). Overexpression of channelrhodopsin-2 interferes with the GABAb receptor-mediated depression of GABA release from the somatostatin-containing interneurons of the prefrontal cortex. Neurophotonics *5*, 25003.

61. Cadwell, C.R., Palasantza, A., Jiang, X., Berens, P., Deng, Q., Yilmaz, M., Reimer, J., Shen, S., Bethge, M., Tolias, K.F., et al. (2016). Electrophysiological, transcriptomic and morphologic profiling of single neurons using Patch-seq. Nat. Biotechnol. *34*, 199–203.

62. Fuzik, J., Zeisel, A., Máté, Z., Calvigioni, D., Yanagawa, Y., Szabó, G., Linnarsson, S., and Harkany, T. (2016). Integration of electrophysiological recordings with single-cell RNA-seq data identifies neuronal subtypes. Nat. Biotechnol. *34*, 175–183.

63. Cadwell, C.R., Scala, F., Li, S., Livrizzi, G., Shen, S., Sandberg, R., Jiang, X., and Tolias, A.S. (2017). Multimodal profiling of single-cell morphology, electrophysiology, and gene expression using Patch-seq. Nat. Protoc. *12*, 2531–2553.

64. Picelli, S., Faridani, O.R., Björklund, A.K., Winberg, G., Sagasser, S., and Sandberg, R. (2014). Full-length RNA-seq from single cells using Smart-seq2. Nat. Protoc. *9*, 171–181.

65. Scala, F., Kobak, D., Bernabucci, M., Bernaerts, Y., Cadwell, C.R., Castro, J.R., Hartmanis, L., Jiang, X., Laturnus, S., Miranda, E., et al. (2021). Phenotypic variation of transcriptomic cell types in mouse motor cortex. Nature *598*, 144–150.

66. Lun, A.T.L., McCarthy, D.J., and Marioni, J.C. (2016). A step-by-step workflow for low-level analysis of single-cell RNA-seq data with Bioconductor. F1000Research *5*, 2122.

67. Amezquita, R.A., Lun, A.T.L., Becht, E., Carey, V.J., Carpp, L.N., Geistlinger, L., Marini, F., Rue-Albrecht, K., Risso, D., Soneson, C., et al. (2020). Orchestrating single-cell analysis with Bioconductor. Nat. Methods *17*, 137–145.

68. Lun, A.T.L., Bach, K., and Marioni, J.C. (2016). Pooling across cells to normalize single-cell RNA sequencing data with many zero counts. Genome Biol. *17*, 75.

69. Saliba, A.-E., Westermann, A.J., Gorski, S.A., and Vogel, J. (2014). Single-cell RNA-seq: advances and future challenges. Nucleic Acids Res. *42*, 8845–8860.

70. Ge, S.X., Jung, D., and Yao, R. (2020). ShinyGO: a graphical gene-set enrichment tool for animals and plants. Bioinformatics *36*, 2628–2629.

71. Engholm-Keller, K., and Larsen, M.R. (2016). Improving the phosphoproteome coverage for limited sample amounts using TiO2-SIMAC-HILIC (TiSH) phosphopeptide enrichment and fractionation. Methods Mol. Biol. *1355*, 161–177.

72. Müller, J.A., Betzin, J., Santos-Tejedor, J., Mayer, A., Oprişoreanu, A.-M., Engholm-Keller, K., Paulußen, I., Gulakova, P., McGovern, T.D., Gschossman, L.J., et al. (2022). A presynaptic phosphosignaling hub for lasting homeostatic plasticity. Cell Rep. *39*, 110696.

73. Peterson, A.C., Russell, J.D., Bailey, D.J., Westphall, M.S., and Coon, J.J. (2012). Parallel reaction monitoring for high resolution and high mass accuracy quantitative, targeted proteomics. Mol. Cell. Proteomics: MCP *11*, 1475–1488.

## STAR★METHODS

### KEY RESOURCES TABLE

| REAGENT or RESOURCE | SOURCE | IDENTIFIER |
|---|---|---|
| Antibodies | | |
| Primary antibody rabbit anti-c-fos | Millipore | Cat# PC05; RRID: AB_213451 |
| Primary antibody rabbit anti-parvalbumin | Millipore | Cat# AB15736; RRID: AB_838238 |
| Primary antibody rabbit anti-somatostatin | Peninsula Laboratories | Cat# T-4102; RRID: AB_518613 |
| Primary antibody rabbit anti-snx6 | Invitrogen | Cat# PA5-115946; RRID: AB_2900580 |
| Secondary antibody Alexa Fluor® 647 | Life Technologies, USA | Cat# A-31573; RRID: AB_2536183 |
| Deposited data | | |
| Proteomic Data | PanoramaWeb | ProteomeXchange ID:PXD036547 |
| PatchSeq Data | Github | https://github.com/pedroxroyero/Patch-Seq-analysis-SLK-KD |
| Experimental models: Organisms/strains | | |
| Parvalbumin-Cre mice, Pvalbtm1(cre)Arbr, | Jackson Laboratories | JAX stock #017320 |
| Somatostatin-Cre mice, (SST)-IRES-Cre (SSTtm2.1(cre)Zjh, | Jackson Laboratories | JAX stock #018973 |
| Recombinant DNA | | |
| Vector for IUE | N/A | pAAV-U6-shRNA-CBA-hrGFP |
| Vector for IUE | N/A | pAAV-U6-shRNA-CBA-mRFP |
| shRNA against SLK | inVitrogen Life Technologies | Custom synthesis; see Schoch et al., 2021[14] for sequences |
| pENN.AAV.CamKII0.4.Cre.SV40 | Addgene | Plasmid #105558 |
| hChR2(H134R)-EYFP-WPRE-HGHpA Addgene, plasmid #20298 | Addgene | Plasmid #20298 |
| AAV-EF1a-double floxed-hChR2(H134R)-EYFP-WPRE-HGHpA | Addgene | Plasmid #20298 |
| Software and algorithms | | |
| ImageJ | N/A | https://imagej.nih.gov/ij/ |
| DEsingle | Wang et al., 2019[55] | https://bioconductor.org/packages/release/bioc/html/DEsingle.html |
| Disgenet2r | Pinero et al., 2017[56] | https://www.disgenet.org/static/disgenet2r/disgenet2r.html |
| Skyline 20.1.0.76 | N/A | https://skyline.ms/wiki/home/software/Skyline/page.view?name=default |
| Barrel cortex model | Landau et al., 2016,[12] Egger et al., 2020[20] | https://cortexinsilico.zib.de/ |

### RESOURCE AVAILABILITY

#### Lead contact

- Further information and requests for resources and reagents should be directed to and will be fulfilled by the lead contact, Heinz Beck (Heinz.beck@ukb.uni-bonn.de).

#### Materials availability

- This study did not generate new unique reagents.

#### Data and code availability

- Proteomic data including skyline analysis files and raw MS files are publicly available at PanoramaWeb, ProteomeXchange ID:PXD036547.
- PatchSeq Information can be viewed here - Github repository: https://github.com/pedroxroyero/Patch-Seq-analysis-SLK-KD.
- Any additional information required to reanalyze the data reported in this paper is available from the lead contact upon request.

## EXPERIMENTAL MODEL AND SUBJECT DETAILS

- For animal studies with in-utero electroporation, timed pregnant mice were used at embryonic day 14 (E14). Male C57Bl/6 and female CD1 mice were allowed to mate overnight (Obtained from Charles River).
- In some experiments, wild type CD1 females were bred with homozygous Parvalbumin (Pv)-Cre (Pvalbtm1(cre)Arbr, JAX stock #017320) or heterozygous somatostatin (SST)-IRES-Cre (SSTtm2.1(cre)Zjh, JAX stock #018973) males.
- For proteomic analysis, Male C57Bl6/N mice (Charles River) were used.

## METHOD DETAILS

### Animals

All experimental procedures were conducted in accordance with the federal law of the state of North Rhine-Westphalia, Germany (Project number: AZ84–02.04.2017.A363). Timed pregnant mice were used for in utero electroporations (IUE) at embryonic day 14 (E14). Male C57Bl/6 and female CD1 mice were allowed to mate overnight, and the day of mating was defined as E0. For viral transduction into specific GABAergic interneurons (INs) subtypes, wild type CD1 females were bred with homozygous Parvalbumin (Pv)-Cre (Pvalbtm1(cre)Arbr, JAX stock #017320) or heterozygous somatostatin (SST)-IRES-Cre (SSTtm2.1(cre)Zjh, JAX stock #018973) males. The offspring of SST-IRES-Cre breedings were genotyped using the primers TCAGGTACATGGATCCACTAGTTCT (mutant forward), GAGGTCTGCCAACTCGAAC (wild type forward), and AGTCAAACG CTTGCTCTTCA (common), being classified as heterozygous if amplified fragments at 198 and 257 bp were observed. Mice of both sexes were used for the experiments and assigned to experimental groups based on the electroporated plasmids. Animals were housed under controlled conditions (12 h light-dark cycle, temperature 22 ± 2°C, and humidity 55 ± 10%) with food and water *ad libitum*.

### Generation of constructs

Constructs were generated as described before.[14] The design of shRNA constructs against SLK was based on sequences found in the RNAi Codex database,[57] obtained as oligonucleotides from Invitrogen life technologies, and annealed in 100 mM Tris pH7.5, 1 M NaCl and 10 mM EDTA solution for 10 min at 95°C. Next, samples were inserted into the vectors pAAV-U6-shRNA-CBA-hrGFP/pAAV-U6-shRNA-CBA-mRFP via BamHI and HindIII restriction sites at room temperature. Knockdown using this shRNA effectively downregulates the expression of SLK (Schoch et al. 2021) and its effects can be reversed by rescue experiments using expression of shSLK-resistant hSLK. Moreover, experiments with a kinase-dead SLK mutant (SLK K63R) mimicked the effects of the SLK shRNA treatment (Schoch et al. 2021). This indicates that the effect of shSLK is due to loss of SLK and not due to off-target effects.

### Intraventricular in utero electroporation

In utero electroporation was performed as described before.[14] Time pregnant (E14) CD1 wild-type mice were deeply anesthetized with isoflurane. Ketoprofen (5 mg/kg - Mibe) and Buprenorphine (0.05 mg/kg - Bayer) were used as analgesia. Uterine horns were exposed to inject each embryo once into the lateral ventricle with 1–2 μL DNA with a concentration of 1.5 μg/μL and fast green (1 mg/mL, Sigma, USA) using a pulled and beveled glass capillary (Drummond Scientific, USA) and a microinjector (Picospritzer III, Parker Hannifin Corporation, USA). Five electric pulses with 50 ms duration were applied at 950 ms intervals with a triple-electrode using a CUY21SC Square Wave Electroporator charged to 30 V (Nepa Gene, Japan). Electrode forceps were positioned to IUE cortical progenitor cells in the somatosensory and motor cortex.[58]

### Stereotaxic viral gene transfer

Electroporated animals (3 weeks old) were anesthetized with a fentanyl/midazolam/medetomidine mixture (0.05/5.0/0.5 mg/kg body weight, i.p.) and received ketoprofen as analgesia (5 mg/kg body weight, s.c.). Next, animals were head-fixated in a stereotactic frame while keeping a constant temperature of 37°C using a regulated heating plate (TCAT-2LV, Physitemp). After removal of the head hair and superficial disinfection, the surface was locally anesthetized with a drop of 10% lidocaine and the skull was exposed. The in utero electroporated area was identified by using a dual fluorescent protein flashlight (DFP-1, Nightsea). Then, a hole was carefully opened with a dental drill at the target site and the tip of a precision syringe (cannula size 34G) was stereotactically inserted through the burrhole in order to slowly deliver the virus particles into the brain area of interest. For activation of feedforward inputs, AAV-syn-ChR2-EYFP (250 nL at 50 nL/min) was injected to reach the ventral posterior medial nucleus (VPM) and the posterior-medial complex (POm) of the thalamus of the electroporated hemisphere (AP: −1.7, ML: +/−1.2, DV: −3.6, relative to bregma). For the activation of feedback inputs, a mixed injection (1:1, 250 nL at 50 nL/min) of pENN.AAV.CamKII0.4.Cre.SV40 (Addgene, plasmid #105558) and AAV-EF1a-double floxed-hChR2(H134R)-EYFP-WPRE-HGHpA (Addgene, plasmid #20298) was performed in 3 locations of the identified cortical electroporated area (500 μm apart across the anterior-posterior axis; 300 μm deep from the pia surface). The same approach was used for the specific activation of parvalbumin and somatostatin-expressing INs, but only AAV-EF1a-double floxed-hChR2(H134R)-EYFP-WPRE-HGHpA (Addgene, plasmid #20298) was injected in Pv-cre and SST-IRES-Cre animals. At the end of the surgery, the scalp was stitched and the anesthesia was terminated by injection of the antagonists naloxone/flumazenil/atipamezole (1.2/0.5/2.5 mg/kg body weight, i.p.). Postoperative analgesia was carried out over 3 days with one daily administration of ketoprofen (5 mg/kg body weight, s.c.). *In vitro* patch-clamp recordings were performed 2 to 3 weeks after virus injection.

### Slice preparation

Electroporated animals ranging from age 4 to 6 weeks were decapitated under deep isoflurane anesthesia. The brain was quickly removed and immersed in ice-cold sucrose-containing artificial cerebrospinal fluid (ACSF; in mM: NaCl 60, sucrose 100, KCl 2.5, CaCl2 1, MgCl2 5, NaH2PO4 1.25, D-glucose 20, NaHCO3 26; pH 7.4, 310 mOsmol, equilibrated with 5% $CO_2$:95% $O_2$). 300 μm-thick coronal brain slices were prepared with a vibratome (Microm HM650 V, Thermo Scientific). Slices containing transfected cells in motor and somatosensory cortices were identified and incubated at 35°C in the same solution for 20 min. Then, slices were maintained for at least 1 h and up to 6 h in ACSF (in mM: NaCl 125, KCl 3.5, CaCl2 2, MgCl2 2, NaH2PO4 1.25, D-glucose 15, NaHCO3 26; pH 7.4, 310 mOsmol, equilibrated with 5% $CO_2$:95% $O_2$) at room temperature.

### Electrophysiological recordings

Slices were transferred into a submerged chamber and superfused with carbogen-saturated ACSF (3 mL/min, 35°C). Layer II/III pyramidal cells were visually identified using infrared oblique illumination contrast microscopy in a 60x water immersion objective (Nikon, N60X-NIR Apo, NA1.0W) on an upright microscope (Nikon Eclipse FN1, Tokyo, Japan). Electroporated cells expressing shSLK or control plasmids were identified visually by hrGFP or mRFP fluorescence using a long-life mercury light source and a FITC (EX465-495, DM505, BA515-555; Nikon, Tokyo, Japan) or TRITC filter cube set (EX515-565, DM565, BA550-660; Nikon, Tokyo, Japan), respectively. Recordings were carried out exclusively in somatosensory cortex. The exception were the white matter stimulation experiments, in which a majority of somatosensory cortex neurons were recorded, but also some slices extended into motor cortex. For postsynaptic currents (PSCs) measurements, whole-cell voltage-clamp configuration was established with a cesium-methane-sulfonate based intracellular solution (in mM: cesium methanesulfonate 120, $MgCl_2$ 0.5, 4-(2-hydroxyethyl)-1-piperazineethanesulfonic acid (HEPES) 5, ethylenglycole-bis(2-aminoethylether)-N,N,N′,N′-tetraacetic acid (EGTA) 5, Adenosine 5′-triphosphate disodium salt ($Na_2$-ATP) 5, N-(2,6-Dimethylphenylcarbamoylmethyl) triethylammonium chloride (QX314$Cl^-$) 5; pH adjusted to 7.25 with CsOH, 295 mOsmol). Resistance of the patch pipettes was 4–6 MΩ. Recordings were performed with a Multiclamp 700B (Molecular Devices) and signals were sampled at 20 kHz with a Digidata 1322A (Molecular Devices) controlled by Clampex 10.2 (Molecular Devices). Holding potentials were corrected offline for a liquid junction potential of 10 mV. For pharmacology experiments, it was used 50 μM 6-Cyano-7-nitroquinoxaline-2,3-dione disodium salt (CNQX, Tocris), 200 μM D-(−)-2-Amino-5-phosphonopentanoic acid (D-AP5, Tocris), 10 μM gabazine (SR 95531 hydrobromide, Tocris), 1 μM tetrodotoxin (TTX, Tocris) and 200 μM 4-aminopyridine (4-AP, Sigma Aldrich). All compounds were applied to the ACSF recording solution and continuously perfused for at least 10 min before continuing with the measurements. In all cases, recordings were performed from several brain slices from at least 3 animals per group.

### Electric and optogenetic stimulation

Electrically- and light-evoked PSCs were recorded from layer II/III electroporated neurons (either shSLK or control XFP). Subsequently, an adjacent pyramidal cell (PC) not targeted by the electroporation in the same slice (<50 μm apart, paired-control) was patched and PSCs were evoked without repositioning the stimulation electrode/light fiber. In most cases, only one pair of cells was recorded per slice, in order to ensure that fresh slices with similar duration in the recording chamber were used for each paired recording. The excitatory and inhibitory components of evoked PSCs were separated by clamping the patched cell at the chloride reversal potential (−80 mV, calculated with Nernst equation) and the cation reversal potential (0 mV), respectively. To achieve synaptic activation of patched cells, a concentric bipolar electrode (FHC, USA) was placed in the subcortical white matter and stimuli with increasing intensities were applied until PSCs were evoked in the recorded cell (240.92 ± 38.62 μA average stimulation intensity). The same stimulation intensity was used to evoke PSCs in the adjacent paired-control. Stimulation frequencies ranged from 1 to 30 Hz (10 pulses). For light-based activation of ChR2-expressing cells and axons, we used a diode 473nm laser (LuxX, Omicron) attached to an optical fiber. The end of the light fiber was immediately above the brain slice to illuminate the electroporated cortical area. Light stimuli with different pulse times (0.5–15 ms) and intensities (0.72–20.96 mW) were applied at frequencies ranging from 1 to 50 Hz. In addition, a long light pulse of 500 ms was applied at a holding potential of −80 mV in order to assess whether the current patched cell displayed photocurrents generated by the expression of ChR2 in its own membrane (Figure S3A). Few electroporated cells displayed intrinsic photocurrents, which were not considered for further quantifications.

In the case of the expression of ChR2 in SST-Cre mice, we observed a minority (∼20%) of neurons where no clear SST immunoreactivity could be detected, in line with previous studies. We did not, however, see unspecific expression in excitatory neurons as described in,[59] as light stimulation did not elicit EPSCs (Figures 4C and 4D) and electroporated excitatory cells did not show immunoreactivity to interneuron markers (Figures S6G–S6J). In addition, we do still observe a marked difference between the experiments with the PV-Cre and SST-Cre mouse lines.

### Patch-clamp recording analysis

Amplitudes and kinetics of evoked PSCs were analyzed in Clampfit (Molecular Devices) and using a custom routine programmed in Python. For feedforward input experiments, PSCs evoked at 100% laser output (20.96 mW) with 10 ms pulse time were plotted and analyzed. In the case of feedback inputs, PCSs resulting from the stimulation at 30% laser output (6.45 mW) and 10 ms pulse time were selected for further analyses due to the appearance of a slow component in EPSC decay at higher laser powers. For the light activation of Pv- and SST-expressing INs, PCSs evoked at 30% laser output (6.45 mW) and 10 ms pulse time were plotted and

analyzed. PSCs ratios were computed by dividing the PSC amplitude of XFP or shSLK neurons by the amplitude of their paired-control PC. Excitatory-inhibitory ratios were calculated by dividing the EPSC by the IPSC of each individual recorded cell. The mean deviation of excitatory-inhibitory ratios represents the absolute value of the subtraction of the respective group mean from each individual value. Short-term plasticity features of recorded neurons were assessed by normalizing synaptic responses to the first response evoked by stimulation trains at 10 and 20 Hz. Pair-pulse ratios were obtained by dividing the second to the first response of pair stimulations at different frequencies (5, 10, 20, 30, 50 Hz). For patch-clamp RNAseq experiments, passive membrane properties were calculated with a custom routine programmed in R. The input resistance was obtained from the steady-state current responses to 5 and 10 mV voltage steps (200 ms) from a holding potential of −80 mV. Capacitance was defined as the area under the capacitive peak divided by the amplitude of the applied voltage step. Frequencies and amplitudes of mEPSC and mIPSC were calculated offline with a custom routine programmed in IGOR Pro. mEPSC were detected by calculating the first derivative of current traces and selecting events for which the first derivative was > 5x than the standard deviation of the baseline 0–3 ms before the event. mIPSCs were detected if the difference between the mean current amplitudes in two adjacent moving windows (0.5 ms) was >5 pA. All detected events were assessed by visual inspection and sorted manually.

### Immunohistochemistry

Electroporated animals (4–6 weeks old) were heart perfused with ice-cold 4% paraformaldehyde (PFA). Brains were dissected and transferred into 4% PFA for 48 h at 4°C for post-fixation. 80 μm slices were cut on a vibratome (Microm HM 650 V, Thermo Scientific) and blocked with 0.25% Triton X-100 and 3% BSA in phosphate-buffered saline (PBS) overnight at 4°C. Next, slices were incubated with the primary antibodies rabbit anti-c-fos (1:500, PC05, Millipore), rabbit anti-parvalbumin (1:500, AB15736, Millipore), rabbit anti-somatostatin (1:500, T-4102, Peninsula Laboratories International) or rabbit anti-snx6 (1:100, PA5-115946, Invitrogen) overnight at 4°C. After three washing steps, slices were incubated with the secondary antibody Alexa Fluor 647 (Life Technologies, USA) for 2 h and mounted on glass slides. Controls consisted of the omission of primary antibodies. Counterstaining of brain sections was achieved using 4′,6-diamidino-2-phenylindole (DAPI). Images were acquired with a Leica SP8 Confocal Microscope using a 10X (parvalbumin and somatostatin) or 40X (c-fos, Snx6) objective and quantified manually using ImageJ software.

For the quantification of c-fos and Snx6 immunolabeling, hrGFP signal was used to delimitate the area of electroporated cells and to create a mask that was superposed on the antibody-labeled images. The average pixel intensity of c-fos and Snx6 labeling was quantified in hrGFP contours and normalized by the average intensity of negative controls. Contours displaying an average intensity of c-fos signal 3x higher than the average intensity of negative controls were classified as c-fos positive cells. Parvalbumin and somatostatin quantifications were performed manually across all cortical layers and within electroporated-targeted brain areas. In the somatostatin stainings, we observed extrasomatic accumulations of intensely fluorescent material that were clearly distinct from the membrane-delimited staining of ChR2-eYFP and did not have a correlate in the DAPI staining. These accumulations were not considered somatic staining and therefore not included in the quantification. A similar phenomenon has been observed by other groups following viral overexpression of ChR2-eYFP (Figure 1B in[60]).

### Patch-clamp recordings and RNA collection

Patch-clamp RNA sequencing experiments were performed following an adapted protocol from previous publications consisting of several steps, including whole-cell patch-clamp recordings, aspiration of cell contents, cDNA synthesis, sequencing, and data analysis.[61–63] Several modifications of the aforementioned patch-clamp protocol were applied in order to avoid RNA degradation during sample collection. Preparations and sample handling were executed under a safety hood with strict RNAse-free conditions, using certified RNase-free disposable products and tools and glassware previously treated with RNaseZap (Invitrogen, AM9780). Cells electroporated with XFP or shSLK (and 3 non-electroporated striatal cells for downstream comparisons) were recorded using baked (200°C, 2 h) borosilicate patch pipettes (2–4 MΩ) filled (maximum 1 μL) with an intracellular solution containing (in mM): 123 potassium gluconate, 12 KCl, 10 HEPES, 0.2 EGTA, 4 MgATP, 0.3 NaGTP, 10 sodium phosphocreatine, pH: 7.25. On the day of the experiment, 1 U/μl recombinant RNase inhibitor (Takara, 2313A) and 20 μg/mL glycogen (Sigma-Aldrich, G1767) was added to the intracellular solution in order to preserve and help to collect the RNA from the recorded cell.[63] Slices were kept in a submerged chamber and superfused with carbogen-saturated ACSF with TTX (1 μM). Once the whole-cell configuration was achieved, mEPSCs and mIPSCs were recorded by clamping the cell at −80 mV for 2 min and 0 mV for 30 s, respectively. In addition, voltage steps (200 ms) of 5 and 10 mV from a holding potential of −80 mV were applied in order to determine the passive properties of the cell. After recording the electrophysiological parameters of interest, negative pressure was applied (20–100 mbar for 1–2 min) to aspirate the cell contents into the patch pipette until the cell body dramatically decreased in size. Next, the pipette was quickly removed and the sample was ejected into an RNase-free PCR tube containing 1 μL lysis buffer (40 mM Guanidine hydrochloride, 0.1 μM Smart dT30VN primer, 5 mM dNTPs), which was immediately frozen in liquid nitrogen and stored at −80°C.

### Library preparation, sequencing, and gene alignment

Individual lysed cells were treated according to the Smart-Seq2 library preparation protocol.[64] Preamplified cDNA was quantified and the average size distribution was determined via D5000 assay on a tapestation4200 system (Agilent). Tagmentation and subsequent next-generation sequencing (NGS) library generation were performed using 200 pg of cDNA per sample following the Smart-Seq2 protocol. NGS libraries were quantified by HS dsDNA assay on a Qubit (Invitrogen) and the average size distribution was determined

via D5000 assay on a tapestation4200 system (Agilent). Libraries were equimolarly pooled, clustered at 1.4 pM, and sequenced using SR 75 cycles High Output v2 chemistry on a NextSeq500 system (Illumina). Raw sequencing data were demultiplexed and converted into fastq format using bcl2fastq2 v2.20 and aligned to mouse genome M16 via STAR aligner considering both, exonic and intronic reads.

### Patch-seq analysis

Exonic and intronic aligned reads were added and used to maximize gene counts as reported for other patch-seq datasets.[63,65] Read counts were used to compute basic quality control metrics for each cell, such as library size, total number of expressed genes, and proportion of mitochondrial reads.[66,67] Cells deviating at least three median absolute deviations (MADs) from the median value of any of the metrics were classified as poor-quality samples and removed from the analysis (final number of cells 69; 28 hrGFP, 38 shSLK, 3 striatum).

Read counts were normalized using a library size deconvolution approach.[68] Briefly, read counts of a subset of cells were pooled and then deconvolved to determine size factors for individual cells. Read counts were divided by their specific cell-based size factor. This helps to account for systematic differences in sequencing coverage while considering composition biases originating from differentially expressed genes in group of cells.

To identify changes in gene expression driven by the absence of SLK, we performed differential expression (DE) analysis between the transcriptomic profile of XFP and shSLK neurons. Due to the nature of this type of data, we had to consider some sources of technical bias. First, due to the low concentration and possible low capture efficiency of RNAs in patched cells, read counts can be inflated with zero values, which introduces noise to the data and makes it difficult to find biological differences among groups.[69] Second, since recording and collecting these samples is extremely challenging, we could not collect the high number of cells usually obtained for sc-RNA-seq from dissociated tissues, which also makes our data noisier due to the heterogeneity of individual neurons. To overcome these problems, we used an analysis pipeline specially designed for single-cell data that was shown to work well for datasets with a large number of zero counts.[55] This approach, called DESingle, employs a zero-inflated negative binomial model to estimate the proportion of real biological zero counts and drop-out events. DEsingle classifies DE genes into three categories; genes that have differences only in the proportion of real zeros between groups, genes that are differentially expressed between the groups without significant difference in the proportion of real zeros, and genes that have significant differences in both the proportions of real zeros and the expression abundances between the two groups.[25] We implemented this approach in R using the raw count data since DEsingle applies a median normalization step in its pipeline. Low abundance genes (which are likely to be dominated by zero counts) were removed from the input matrix by choosing genes expressed in at least 28 cells (the size of the smallest experimental group; final number of genes: 3287). Genes with a false discovery rate adjusted p value $\leq$ 0.05 were considered as differentially expressed.

We next investigated whether the DE genes found in SLK-deficient neurons are associated with human diseases. For this purpose, we used Disgenet2r, a platform with a large collection of curated repositories, genome-wide association studies, and scientific publications of genes and variants involved in human pathologies.[56] We explored the total number of different diseases associated with each DE gene across all of the data sources available on the platform and grouped them by disease class. The 10 disease classes with the highest number of diseases associated with DE genes were selected and plotted.

In order to determine the relationship between changes in electrophysiological features and transcriptomic profiles, we applied a sparse reduced-rank regression (RRR) analysis.[26] This approach uses an elastic net regularization implementing lasso and ridge penalties to perform feature selection. We used the 3 electrophysiological properties found to be altered in SLK-deficient neurons (mIPSC frequency, cell capacitance, and input resistance, Figure 7H). The 3000 most abundant genes from the normalized count matrix (see above) were selected. Gene expression and electrophysiological variables were standardized to zero mean and unit variance.

The sparse RRR has two hyperparameters, alpha and lambda. Alpha controls the adjustment between the lasso (alpha = 1) and the ridge (alpha = 0) regularization, while lambda controls the regularization strength and defines the number of genes selected by the model. A 2-fold cross-validation was performed to tune the model and found that alpha = 0.25, lambda = 0.47, and rank = 2 yielded the highest $R^2$ values (Figures S10A–S10C).

The sparse RRR plots display the mapping of the electrophysiological and transcriptomic variables onto the two reduced dimensions. Lines represent correlations of the different electrophysiological and transcriptomic variables with both components. The circle indicates a correlation of 1. For visualization purposes, the transcriptomic space was plotted labeling different relevant gene ontology terms separately. Enriched ontology terms were obtained using ShinyGo and setting the false discovery rate to 0.05.[70]

### Induction of status epilepticus and extraction of hippocampal tissue for targeted mass spectrometry

Male C57Bl6/N mice (Charles River; ~60 days old, weight $\geq$20 g) were injected with 1 mg/kg scopolamine methyl nitrate (Sigma). Twenty minutes later, status epilepticus was induced by subcutaneous injection with 335 mg/kg pilocarpine hydrochloride (Sigma) as described previously (Pitsch et al., 2007; Pitsch et al., 2017). Forty minutes after onset of status epilepticus, mice were subcutaneously injected with diazepam (4 mg/kg; Ratiopharm). Animals were only used in the study if they exhibited behavioral status epilepticus. A modified seizure scheme was used to identify behavioral status epilepticus: sustained convulsions with postural loss (Pitsch et al., 2007; Pitsch et al., 2017). At 4 and 24 h after injection of pilocarpine, both hemispheres of the hippocampus were removed and frozen using dry ice. Tissue was homogenized in 500 μL PBS (45 s), before 125 μL lysis buffer was added [2% SDS,

50 mM trisaminomethane/HCl pH 7.4, 2 mM ethylene glycol-bis(β-aminoethyl ether)-N,N,N0, N0-tetraacetic acid, 2 mM ethylenediaminetetraacetic acid, Complete Protease Inhibitor Cocktail (Roche), 2 mM phenylmethylsulfonyl (Sigma-Aldrich), 5 mM NaF (Sigma-Aldrich), 2 mM beta-glycerophosphate (Sigma-Aldrich), Phosphatase Inhibitor Cocktail 2 (1:1000) and PhosSTOP (Roche)]. Lysates were incubated at 85°C for 10 min and subsequently sonicated for 3 x 10 s. Samples were frozen on dry ice before being lyophilized.

### Targeted mass spectrometry analysis of SLK phosphorylation and protein levels

The lyophilized samples were resuspended in a 100 μL solution of 10 mM tris(2-carboxyethyl) phosphine, reduced for 10 min at 85°C and subsequently alkylated in 25 mM iodoacetamide at 22°C in the dark. Proteins were precipitated from the samples using chloroform-methanol extraction and air dried. The precipitates were dissolved in 20 μL solution containing 7.8 M urea, 50 mM triethylammonium bicarbonate (TEAB), and 5 μg of Lys-C (FUJIFILM Wako Pure Chemical Corporation) for 8-h digestion at 25°C. The samples were diluted with a solution containing 170 μL 100 mM 4-[2-hydroxyethyl]-1-piperazineethanesulfonic acid (HEPES) (pH 8) and 5 μg TrypZean trypsin (Sigma) for subsequent digestion at 37°C for 4 h. The trypsin digestion was repeated with an additional 5 μg for 4 h under the same conditions. Approximately 600 μg of each sample was purified by solid phase extraction (Oasis 30 mg sorbent, Waters) and enriched for phosphopeptides using titanium dioxide enrichment as previously described.[71] The unbound peptide was collected and used to analyze the non-phosphorylated peptide.

Each phosphopeptide sample consisting of one-third of the material purified material in 5 μL was injected into a Dionex UltiMate 3000 RSLC nano system and analyzed by a Q Exactive Plus hybrid quadrupole-orbitrap mass spectrometer (Thermo Fisher Scientific). The column was 300 × 0.075 mm fused silica with a pulled tip and packed with ReproSil Pur C18 AQ 1.9 μm resin (Dr Maisch, Germany). The electrospray conditions were as described previously.[72] The sample was loaded in 99% buffer A (0.1% formic acid in water) and 1% buffer B (0.1% formic acid, 90% acetonitrile, 9.9% water) for 25 min at 300 nL/min, then the gradient was to 5% B in 1 min at 250 nL/min, to 25% B in 74 min, to 35% B in 8 min, to 99% B in 1 min, held at 99% B for 2 min before returning to 1% B in 1 min and held at 99% B for 8 min whilst the flow rate was increased to 300 nL/min for equilibration. Parallel reaction monitoring MS[73] was performed for 120 min. The MS/MS resolution was 70,000, the automatic gain control target was 3,000,000, the maximum ion time was 220 ms, the isolation window was 0.7 m/z and the normalised collision energy was 30. Approximately 2500 ng of non-phosphopeptide in 3.5 μL was injected using a different gradient for analysis. The sample loading was in 99% A for 17.5 min at 300 nL/min, then the gradient was to 6% B in 1 min at 250 nL/min, to 28% B in 101.5 min, and then the gradient continued the same as for phosphopeptides to a total length 140 min. The parallel reaction monitoring MS settings were the same as for phosphopeptides. Phosphopeptides and non-phosphopeptides were selected from previous analyses in our laboratory and from public databases. Three phosphopeptides that have stable levels of phosphorylation in a selection of mouse phosphoproteomic studies were included for normalisation. Two peptides from tubulin alpha-4A chain and four peptides from cytoplasmic dynein 1 heavy chain 1 were included as loading controls. Each peptide was targeted within a 12 min or wider retention time window. All MS files were searched using MaxQuant 1.6.7.0 to create a library of search results as evidence of correct identification and retention time. Within MaxQuant, the Mus musculus reference proteome with 55,315 entries, downloaded from UniProt on August 11 2022, was used, as well as the in-built contaminants fasta file. Oxidation of Met, acetylation of N-terminal residues, phosphorylation of Ser/Thr/Tyr and deamidation of Asn/Gln were variable modifications and carbamidomethylation of Cus was a fixed modification. The minimum peptide length was 6, trypsin/P was used for enzyme specificity with a maximum of 2 missed cleavages. All other MaxQuant settings were default. The MaxQuant msms.txt output file and the raw files were examined in Skyline 20.1.0.76. Five or more fragment ions and a maximum of 2 ppm mass accuracy were required for each peptide. The quantitative values for each peptide were exported to Excel and the peptide intensities were normalised to the loading controls. The data was then exported to Prism 9.0.2 for statistical analysis. Multiple unpaired t-tests were performed and the p value was adjusted with a false discovery rate of 5%. All data with an adjusted p value >0.05 was considered significant. The Skyline analysis files and raw MS files are publicly available at PanoramaWeb, ProteomeXchange ID:PXD036547, URL.

### Computational modeling

We performed simulations of PC activity in response to anatomically and functionally well-constrained synaptic input, as reported previously for simulations of sensory-evoked activity in Layer IV (Landau et al., 2016) and Layer V (Egger et al., 2020) of the rat barrel cortex. In short, the constraints for the numbers and dendritic distributions of cell type-specific synapses that impinge onto the PC models are based on an anatomically realistic network model (Egger et al., 2014; Udvary et al., 2022). PCs received input from all intracortical excitatory and inhibitory cell types in the barrel cortex, as well as from neurons in the primary thalamus, which were activated in accordance with cell type-specific spontaneous and sensory-evoked activity measured *in vivo* by (Kock et al., 2007) for passive single whisker deflection.

We simulated all PCs in layer II/III of the C2 barrel column (n = 2486). Each PC was represented by a generalized linear model (GLM) (Weber and Pillow, 2017) to simulate synaptic integration and action potential generation. GLM models were fitted to biophysically-detailed multi-compartmental models of PCs and predicted their spiking output accurately (AUROC >0.9) for the investigated synaptic input patterns with 1 ms resolution. The GLM models use a separate stimulus filter for excitatory and inhibitory synapses where each filter weights synapses according to their soma distance along the dendrites and time point of activation. The sum of these filtered synaptic input patterns reflects the net excitation (NE) the cell receives at any given time point. The NE is then passed through

a sigmoidal nonlinearity to determine the spiking probability, and outputs are stochastically generated based on this probability. To account for the refractory period, we apply a penalty to the NE for a short time period after a spike occurred.

Next, we adjusted the strength of inhibitory synapses. We simulated 10 s of spontaneous synaptic input to all PCs, and recorded their mean spike rate, mean NE value, and the contribution of excitatory and inhibitory inputs to the NE. There is a clear relationship between mean NE and spike rate, which we used to select a target mean NE. We calculated for each PC the scale factor for inhibitory inputs to attain the target NE value – this is the value used for cell-autonomous inhibitory adjustment. The mean of all cell autonomous scale factors was used as the value for global inhibitory adjustment.

We simulated 60 s of spontaneous activity and 100 whisker stimulus trials for networks in which all inhibitory synapses were adjusted globally, and for networks in which all inhibitory synapses were adjusted cell autonomously. We recorded spike times for all PCs, and calculated the ratio of excitation to inhibition received by each PC during spontaneous activity. Finally, we performed a sensitivity analysis to explore the effect of the fraction of inhibitory cells subject to cell-autonomous synaptic strength adjustment by PCs (from 0% to 100%).

### Open field behavior

Mice were tracked in a transparent arena used for the gridwalking test (20 × 30 $cm^2$) and allowed to explore the arena for 15 min once a week. The analysis of video tracking data was performed with Ethovision XT software (vers. 14.0, Noldus) and built-in procedures. For open field, the position of the animal was identified with regard to a virtual center region that had a distance of 7 cm to the walls. The time the animal spent in this center region and the number of entries was calculated for every 5 min trial, together with the total distance traveled (m) and the mean velocity (cm/s).

## QUANTIFICATION AND STATISTICAL ANALYSIS

Patch-clamp data were analyzed in Clampfit (Molecular Devices) and using a custom routine programmed in Python. Statistical analysis for Mass Spectrometry as performed with Skyline 20.1.0.76, and with GraphPad Prism 9.0.2. Statistical analysis for patch Seq datasets were performed in R and python using published analysis routines as indicated (code available on https://github.com/pedroxroyero/Patch-Seq-analysis-SLK-KD), as well as published analysis routines (DEsingle, Disgenet2r). Immunohistochemical data were analyzed with ImageJ. Datasets were assessed for normality parameters prior to significance determination. Values are expressed as means ± standard error of the mean in the text and in the figures. N numbers for both animals and cells are given in the main text or figure legends Statistical tests and p values are indicated in the main text or in the figure legend.

**Cell Reports, Volume *41***

## Supplemental information

# Circuit-selective cell-autonomous regulation of inhibition in pyramidal neurons by Ste20-like kinase

**Pedro Royero, Anne Quatraccioni, Rieke Früngel, Mariella Hurtado Silva, Arco Bast, Thomas Ulas, Marc Beyer, Thoralf Opitz, Joachim L. Schultze, Mark E. Graham, Marcel Oberlaender, Albert Becker, Susanne Schoch, and Heinz Beck**

**Supplementary Information**

| | XFP | shSLK |
|---|---|---|
| mIPSC amplitude (pA) | 19.44 ± 0.79 | 17.72 ± 0.63 |
| mEPSC amplitude (pA) | 12.93 ± 0.62 | 12.87 ± 0.32 |
| mEPSC frequency (Hz) | 1.89 ± 0.22 | 1.54 ± 0.23 |
| Holding currents (pA) | -112.79 ± 15.41 | -88.50 ± 18.93 |

**Supplementary Table S1.** Miniature postsynaptic currents and passive membrane properties of SLK-KD neurons. Asterisk indicates significance in unpaired t-test ($p$=0.031, input resistance).

| Gene name | Norm. fold change | Desingle DE type |
|---|---|---|
| Cdr1 | 0.046 | DEg |
| 1700034P13Rik | 0.211 | DEa |
| Spock2 | 16.718 | DEa |
| Reep5 | 0.224 | DEa |
| Zfp106 | 44.046 | DEg |
| Aco1 | 0.136 | DEg |
| Rn7sk | 0.098 | DEg |
| Pgm2l1 | 16.749 | DEg |
| Gpx4-ps2 | 2.772 | DEa |
| Smarcc2 | 0.039 | DEg |
| AU040320 | 8.982 | DEg |
| Arglu1 | 4.076 | DEg |
| Gopc | 0.283 | DEg |
| Ddx6 | 7.014 | DEa |
| Tax1bp1 | 19.712 | DEg |
| Slmap | 4.718 | DEg |
| Phf20l1 | 5.178 | DEg |
| Snx6 | 0.055 | DEa |
| Sgms1 | 7.705 | DEg |
| Vps4a | 14.050 | DEg |
| Dctn4 | 0.359 | DEa |
| Megf9 | 2.870 | DEg |
| Son | 3.393 | DEg |
| Amd2 | 0.111 | DEg |

**Supplementary Table S2.** Genes differentially expressed genes in shSLK neurons. Using a zero-inflated negative binomial model with DEsingle, we found 24 differentially expressed genes in shSLK compared to XFP neurons. DEsingle classifies genes with altered expression profiles into three categories: DEs (different expression status), DEa (different expression abundance), and DEg (general differential expression), depending on whether the genes showed differences in the proportion of cells with zero counts, the actual RNA abundance or both, respectively.

| Gene name | Gene description |
|---|---|
| Prpf6 | pre-mRNA splicing factor 6 |
| Pde1c | phosphodiesterase 1C |
| Snx6 | sorting nexin 6 |
| Eif1b | eukaryotic translation initiation factor 1B |
| Psmd2 | proteasome (prosome, macropain) 26S subunit, non-ATPase, 2 |
| Hnrnph1 | heterogeneous nuclear ribonucleoprotein H1 |
| Nav1 | neuron navigator 1 |
| Klhl3 | kelch-like 3 |
| Eef1a2 | eukaryotic translation elongation factor 1 alpha 2 |
| Mpped2 | metallophosphoesterase domain containing 2 |
| Coa3 | cytochrome C oxidase assembly factor 3 |
| Cacnb4 | calcium channel, voltage-dependent, beta 4 subunit |
| Mgat4c | MGAT4 family, member C |
| Phykpl | 5-phosphohydroxy-L-lysine phospholyase |
| Adcy1 | adenylate cyclase 1 |
| Arf5 | ADP-ribosylation factor 5 |
| Strn3 | striatin, calmodulin binding protein 3 |
| Unc79 | unc-79 homolog |
| Nsd1 | nuclear receptor-binding SET-domain protein 1 |
| Dapk1 | death associated protein kinase 1 |
| Kif2a | kinesin family member 2A |
| Ptprg | protein tyrosine phosphatase, receptor type, G |
| Prkn | parkin RBR E3 ubiquitin protein ligase |
| Vti1a | vesicle transport through interaction with t-SNAREs 1A |
| Arhgdia | Rho GDP dissociation inhibitor (GDI) alpha |
| Zfhx4 | zinc finger homeodomain 4 |
| Chid1 | chitinase domain containing 1 |
| Rpl14 | ribosomal protein L14 |
| Uimc1 | ubiquitin interaction motif containing 1 |
| Epha4 | Eph receptor A4 |
| Ptpn4 | protein tyrosine phosphatase, non-receptor type 4 |
| Srgap2 | SLIT-ROBO Rho GTPase activating protein 2 |
| Frmd4a | FERM domain containing 4A |
| Sema6d | sema domain, transmembrane domain (TM), and cytoplasmic domain, (semaphorin) 6D |
| Mtch2 | mitochondrial carrier 2 |
| Vps16 | VSP16 CORVET/HOPS core subunit |
| Gnas | GNAS (guanine nucleotide binding protein, alpha stimulating) complex locus |
| Nbea | neurobeachin |
| Elavl4 | ELAV like RNA binding protein 4 |
| Csmd2 | CUB and Sushi multiple domains 2 |
| Sema3a | sema domain, immunoglobulin domain (Ig), short basic domain, secreted, (semaphorin) 3A |
| Gcc1 | golgi coiled coil 1 |
| Copg1 | coatomer protein complex, subunit gamma 1 |
| Foxp1 | forkhead box P1 |
| Cntn3 | contactin 3 |
| Tial1 | Tia1 cytotoxic granule-associated RNA binding protein-like 1 |
| Sh3bgrl | SH3-binding domain glutamic acid-rich protein like |
| Dnaja2 | DnaJ heat shock protein family (Hsp40) member A2 |
| Cadm1 | cell adhesion molecule 1 |
| Dpyd | dihydropyrimidine dehydrogenase |
| Mga | MAX gene associated |
| Ube2f | ubiquitin-conjugating enzyme E2F |
| Slc2a13 | solute carrier family 2 (facilitated glucose transporter), member 13 |
| Mar-01 | membrane-associated ring finger (C3HC4) 1 |
| Cdh8 | cadherin 8 |
| Rsrp1 | arginine/serine rich protein 1 |
| 4932438A13Rik | RIKEN cDNA 4932438A13 gene |
| Atp11b | ATPase, class VI, type 11B |

| | |
|---|---|
| Mphosph9 | M-phase phosphoprotein 9 |
| Btbd10 | BTB (POZ) domain containing 10 |
| Mical2 | microtubule associated monooxygenase, calponin and LIM domain containing 2 |
| Trpm4 | transient receptor potential cation channel, subfamily M, member 4 |
| Herc1 | HECT and RLD domain containing E3 ubiquitin protein ligase family member 1 |
| Plcl2 | phospholipase C-like 2 |
| Cdh6 | cadherin 6 |
| Ncam1 | neural cell adhesion molecule 1 |
| Gabbr2 | gamma-aminobutyric acid (GABA) B receptor, 2 |
| Flywch1 | FLYWCH-type zinc finger 1 |
| Btaf1 | B-TFIID TATA-box binding protein associated factor 1 |
| 1110051M20Rik | RIKEN cDNA 1110051M20 gene |
| Atp1a3 | ATPase, Na+/K+ transporting, alpha 3 polypeptide |
| Sox5 | SRY (sex determining region Y)-box 5 |
| Myrip | myosin VIIA and Rab interacting protein |
| Mat2b | methionine adenosyltransferase II, beta |
| Usp22 | ubiquitin specific peptidase 22 |
| Fam221b | family with sequence similarity 221, member B |
| Adgrd1 | adhesion G protein-coupled receptor D1 |
| Osbpl1a | oxysterol binding protein-like 1A |
| Chrm3 | cholinergic receptor, muscarinic 3, cardiac |
| Lyrm4 | LYR motif containing 4 |
| Rpl14-ps1 | ribosomal protein L14, pseudogene 1 |
| Gpr85 | G protein-coupled receptor 85 |
| Fbxl13 | F-box and leucine-rich repeat protein 13 |
| Acap2 | ArfGAP with coiled-coil, ankyrin repeat and PH domains 2 |
| Grm5 | glutamate receptor, metabotropic 5 |
| Adarb2 | adenosine deaminase, RNA-specific, B2 |
| Prkcb | protein kinase C, beta |
| Nyap2 | neuronal tyrosine-phophorylated phosphoinositide 3-kinase adaptor 2 |
| Fez2 | fasciculation and elongation protein zeta 2 (zygin II) |
| Kcnq3 | potassium voltage-gated channel, subfamily Q, member 3 |
| Slit3 | slit guidance ligand 3 |
| 5730455P16Rik | RIKEN cDNA 5730455P16 gene |
| Ntrk3 | neurotrophic tyrosine kinase, receptor, type 3 |
| Hnrnpm | heterogeneous nuclear ribonucleoprotein M |
| Caln1 | calneuron 1 |
| Fhit | fragile histidine triad gene |
| Ctnna3 | catenin (cadherin associated protein), alpha 3 |
| Galnt13 | polypeptide N-acetylgalactosaminyltransferase 13 |
| Agbl4 | ATP/GTP binding protein-like 4 |
| Ctnna2 | catenin (cadherin associated protein), alpha 2 |
| Nol7 | nucleolar protein 7 |
| Unc5d | unc-5 netrin receptor D |
| Cacng3 | calcium channel, voltage-dependent, gamma subunit 3 |
| Macrod2 | MACRO domain containing 2 |
| Dok6 | docking protein 6 |
| Syndig1 | synapse differentiation inducing 1 |
| Serf2 | small EDRK-rich factor 2 |
| Scn2a | sodium channel, voltage-gated, type II, alpha |
| Chd2 | chromodomain helicase DNA binding protein 2 |
| Nwd2 | NACHT and WD repeat domain containing 2 |
| Malat1 | metastasis associated lung adenocarcinoma transcript 1 (non-coding RNA) |
| Syne1 | spectrin repeat containing, nuclear envelope 1 |

**Supplementary Table S3.** List of genes selected by the sparse reduced-rank regression model that best predict the electrophysiological features found to be altered in SLK-KD neurons in a reduced space.

| Pathway | Enrichment FDR | N° Genes | Pathway Genes | Fold Enrichment | Gene names |
|---|---|---|---|---|---|
| Cell morphogenesis | 0.002476 | 18 | 1056 | 3.519243 | Adcy1 Prkn Arhgdia Epha4 Srgap2 Sema6d Elavl4 Sema3a Foxp1 Cadm1 Cdh8 Cdh6 Nyap2 Slit3 Ntrk3 Ctnna2 Unc5d Syne1 |
| Regulation of membrane potential | 0.002476 | 12 | 449 | 5.517922 | Cacnb4 Prkn Mtch2 Foxp1 Trpm4 Atp1a3 Grm5 Kcnq3 Ntrk3 Ctnna3 Scn2a Syne1 |
| Cellular response to amyloid-beta | 0.009276 | 4 | 36 | 22.94025 | Snx6 Epha4 Atp1a3 Grm5 |
| Trans-synaptic signaling | 0.010876 | 13 | 707 | 3.796336 | Cacnb4 Adcy1 Prkn Epha4 Elavl4 Cadm1 Cdh8 Plcl2 Chrm3 Grm5 Prkcb Cacng3 Syne1 |
| Action potential | 0.012498 | 6 | 137 | 9.042143 | Cacnb4 Foxp1 Trpm4 Ntrk3 Ctnna3 Scn2a |
| Nervous system development | 0.012498 | 26 | 2409 | 2.228318 | Nav1 Adcy1 Kif2a Prkn Epha4 Srgap2 Sema6d Elavl4 Sema3a Foxp1 Cntn3 Cadm1 Herc1 Atp1a3 Sox5 Grm5 Nyap2 Slit3 Ntrk3 Agbl4 Ctnna2 Unc5d Macrod2 Syndig1 Scn2a Syne1 |
| Chemical synaptic transmission | 0.018022 | 12 | 699 | 3.544417 | Cacnb4 Adcy1 Prkn Epha4 Elavl4 Cdh8 Plcl2 Chrm3 Grm5 Prkcb Cacng3 Syne1 |
| Regulation of localization | 0.018022 | 28 | 2821 | 2.049253 | Pde1c Cacnb4 Adcy1 Dapk1 Kif2a Prkn Arhgdia Epha4 Srgap2 Frmd4a Sema6d Gnas Sema3a Foxp1 Trpm4 Myrip Chrm3 Grm5 Prkcb Kcnq3 Ntrk3 Hnrnpm Ctnna3 Ctnna2 Unc5d Cacng3 Scn2a Syne1 |
| Synaptic transmission, glutamatergic | 0.018022 | 5 | 102 | 10.1207 | Cacnb4 Prkn Cdh8 Grm5 Cacng3 |
| Neuron projection development | 0.021026 | 15 | 1064 | 2.910652 | Adcy1 Prkn Epha4 Srgap2 Sema6d Elavl4 Sema3a Foxp1 Herc1 Nyap2 Slit3 Ntrk3 Ctnna2 Unc5d Syne1 |
| Neuron migration | 0.025618 | 6 | 180 | 6.882075 | Nav1 Srgap2 Sema3a Ntrk3 Ctnna2 Unc5d |
| Cell-cell signaling | 0.026338 | 18 | 1496 | 2.484172 | Pde1c Cacnb4 Adcy1 Prkn Epha4 Gnas Elavl4 Cadm1 Cdh8 Trpm4 Plcl2 Gabbr2 Myrip Chrm3 Grm5 Prkcb Cacng3 Syne1 |
| Central nervous system neuron differentiation | 0.026338 | 6 | 186 | 6.660073 | Epha4 Elavl4 Sema3a Herc1 Sox5 Agbl4 |
| Generation of neurons | 0.026338 | 19 | 1627 | 2.411053 | Nav1 Adcy1 Prkn Epha4 Srgap2 Sema6d Elavl4 Sema3a Foxp1 Herc1 Sox5 Grm5 Nyap2 Slit3 Ntrk3 Agbl4 Ctnna2 Unc5d Syne1 |
| Regulation of biological quality | 0.026338 | 33 | 3751 | 1.816384 | Pde1c Klhl3 Cacnb4 Adcy1 Prkn Arhgdia Epha4 Sema6d Mtch2 Gnas Nbea Elavl4 Sema3a Foxp1 Cdh8 Atp11b Trpm4 Plcl2 Atp1a3 Myrip Chrm3 Grm5 Prkcb Kcnq3 Ntrk3 Hnrnpm Ctnna3 Ctnna2 Cacng3 Syndig1 Serf2 Scn2a Syne1 |

**Supplementary Table S4.** Enriched gene ontology terms related to cellular biological process.

| Pathway | Enrichment FDR | N° Genes | Pathway Genes | Fold Enrichment | Genes |
|---|---|---|---|---|---|
| Neuron projection | 6.37E-08 | 29 | 1561 | 3.835622 | Nav1 Strn3 Prkn Vti1a Epha4 Srgap2 Vps16 Gnas Elavl4 Sema3a Cntn3 Cadm1 Slc2a13 Cdh8 Gabbr2 Atp1a3 Myrip Chrm3 Grm5 Prkcb Fez2 Kcnq3 Ntrk3 Agbl4 Ctnna2 Cacng3 Syndig1 Scn2a Syne1 |
| Synapse | 1.40E-06 | 25 | 1465 | 3.523247 | Eef1a2 Cacnb4 Adcy1 Prkn Vti1a Arhgdia Rpl14 Epha4 Srgap2 Nbea Elavl4 Cadm1 Cdh8 Gabbr2 Atp1a3 Myrip Chrm3 Grm5 Prkcb Ntrk3 Ctnna2 Cacng3 Syndig1 Scn2a Syne1 |
| Axon | 1.53E-06 | 18 | 770 | 4.826391 | Nav1 Prkn Epha4 Vps16 Elavl4 Sema3a Cadm1 Slc2a13 Cdh8 Atp1a3 Chrm3 Prkcb Fez2 Kcnq3 Ntrk3 Agbl4 Ctnna2 Scn2a |
| Somatodendritic compartment | 7.12E-06 | 20 | 1076 | 3.837589 | Pde1c Eef1a2 Strn3 Prkn Vti1a Epha4 Srgap2 Vps16 Gnas Elavl4 Sema3a Cadm1 Trpm4 Atp1a3 Chrm3 Grm5 Kcnq3 Cacng3 Syndig1 Syne1 |
| Cell junction | 1.24E-05 | 28 | 2069 | 2.794076 | Eef1a2 Cacnb4 Adcy1 Prkn Vti1a Arhgdia Rpl14 Epha4 Srgap2 Frmd4a Nbea Elavl4 Cadm1 Cdh8 Cdh6 Gabbr2 Atp1a3 Myrip Chrm3 Grm5 Prkcb Ntrk3 Ctnna3 Ctnna2 Cacng3 Syndig1 Scn2a Syne1 |
| Postsynapse | 1.53E-05 | 16 | 737 | 4.48222 | Adcy1 Prkn Rpl14 Epha4 Srgap2 Nbea Cadm1 Gabbr2 Atp1a3 Chrm3 Grm5 Ntrk3 Ctnna2 Cacng3 Syndig1 Syne1 |
| Glutamatergic synapse | 6.97E-05 | 12 | 474 | 5.226893 | Cacnb4 Adcy1 Epha4 Elavl4 Cadm1 Cdh8 Gabbr2 Chrm3 Grm5 Ntrk3 Cacng3 Scn2a |
| Golgi apparatus | 9.88E-05 | 21 | 1449 | 2.992207 | Mgat4c Arf5 Strn3 Prkn Vti1a Chid1 Epha4 Sema6d Gnas Nbea Gcc1 Copg1 Marchf1 Atp11b Mphosph9 Trpm4 Atp1a3 Caln1 Galnt13 Agbl4 Syne1 |
| Presynapse | 0.000137 | 13 | 610 | 4.400015 | Cacnb4 Prkn Vti1a Epha4 Cadm1 Cdh8 Gabbr2 Atp1a3 Chrm3 Prkcb Ctnna2 Syndig1 Scn2a |
| Dendritic tree | 0.000298 | 14 | 772 | 3.744134 | Strn3 Epha4 Srgap2 Gnas Elavl4 Sema3a Cadm1 Atp1a3 Chrm3 Grm5 Kcnq3 Cacng3 Syndig1 Syne1 |
| Cell body | 0.000429 | 14 | 806 | 3.586193 | Pde1c Eef1a2 Strn3 Prkn Vti1a Epha4 Vps16 Gnas Elavl4 Slc2a13 Trpm4 Atp1a3 Kcnq3 Syndig1 |
| Dendritic spine head | 0.000464 | 3 | 14 | 44.24191 | Srgap2 Atp1a3 Syne1 |

**Supplementary Table S5.** Enriched gene ontology terms related to cellular component.

| **Distance moved** | F | P value |
|---|---|---|
| Time (sessions) | $F_{(4, 151)} = 59.78$ | <0,0001 |
| Control vs. shSLK | $F_{(1, 38)} = 1.24$ | 0.27 |
| Time x SLK kd | $F_{(4, 151)} = 0.39$ | 0.82 |
| **Mean velocity** | | |
| Time (sessions) | $F_{(4, 151)} = 59.80$ | <0,0001 |
| Control vs. shSLK | $F_{(1, 38)} = 1.232$ | 0.27 |
| Time x SLK kd | $F_{(4, 151)} = 0.3858$ | 0.82 |
| **In center (frequency)** | | |
| Time (sessions) | $F_{(4, 151)} = 63..64$ | <0,0001 |
| Control vs. shSLK | $F_{(1, 38)} = 0.18$ | 0.67 |
| Time x SLK kd | $F_{(4, 151)} = 0.28$ | 0.89 |
| **In center (duration)** | | |
| Time (sessions) | $F_{(4, 151)} = 14.78$ | <0,0001 |
| Control vs. shSLK | $F_{(1, 38)} = 1.20$ | 0.28 |
| Time x SLK kd | $F_{(4, 151)} = 0.34$ | 0.85 |

**Supplementary Table S6.** Two-way ANOVA results for open field behavior, see Supplementary Fig. S9.

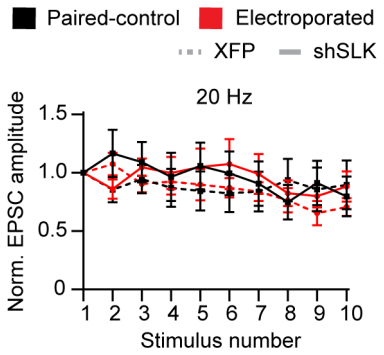


**Figure S1: SLK-deficient neurons do not display changes in excitatory short-term plasticity after repetitive electrical activation.** EPSC amplitudes (normalized to first response) of synaptic responses evoked by white matter electrical stimulation trains at 20 Hz of neurons expressing shSLK or control XFP compared to their respective, adjacent paired-control PCs. Data are represented as mean ± SEM.

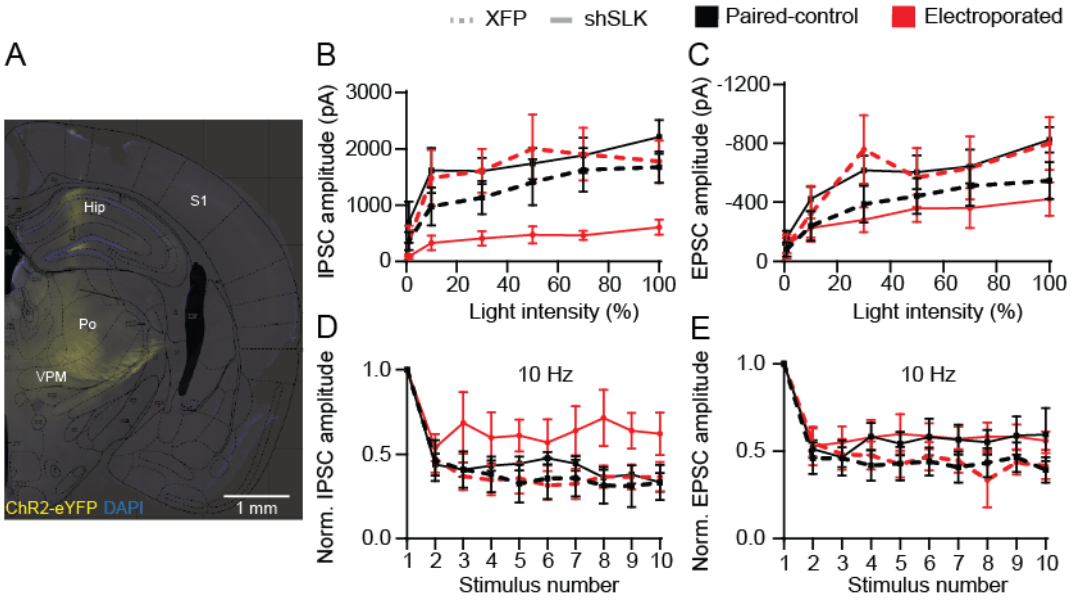


**Figure S2: Light-based activation of thalamic axons revealed disrupted feed-forward inhibition in shSLK neurons. A,** Representative micrograph showing ventral posteromedial (VPM) and posterior thalamic nuclei (Po) expressing ChR2-eYFP 2 weeks after intracranial injection of a ChR2-expressing virus. The image is overlapped with a schematic brain slice from Paxinos and Franklin (2001). The dorsal hippocampus (Hip) and primary somatosensory cortex (S1) can also be observed. **B, C,** Amplitudes of light-evoked feed-forward IPSCs (B) and EPSCs (C) across different light stimulation intensities (100% = 20.96 mW light fiber output) in neurons expressing shSLK or control XFP compared to their respective, adjacent paired-control PCs. **D, E,** IPSC (D) and EPSC (E) amplitudes (normalized to first response) of synaptic responses evoked by light-based stimulation trains at 10 Hz of ChR2-expressing thalamic axons in neurons expressing shSLK or control XFP compared to their respective, adjacent paired-control PCs. Data are represented as mean ± SEM.

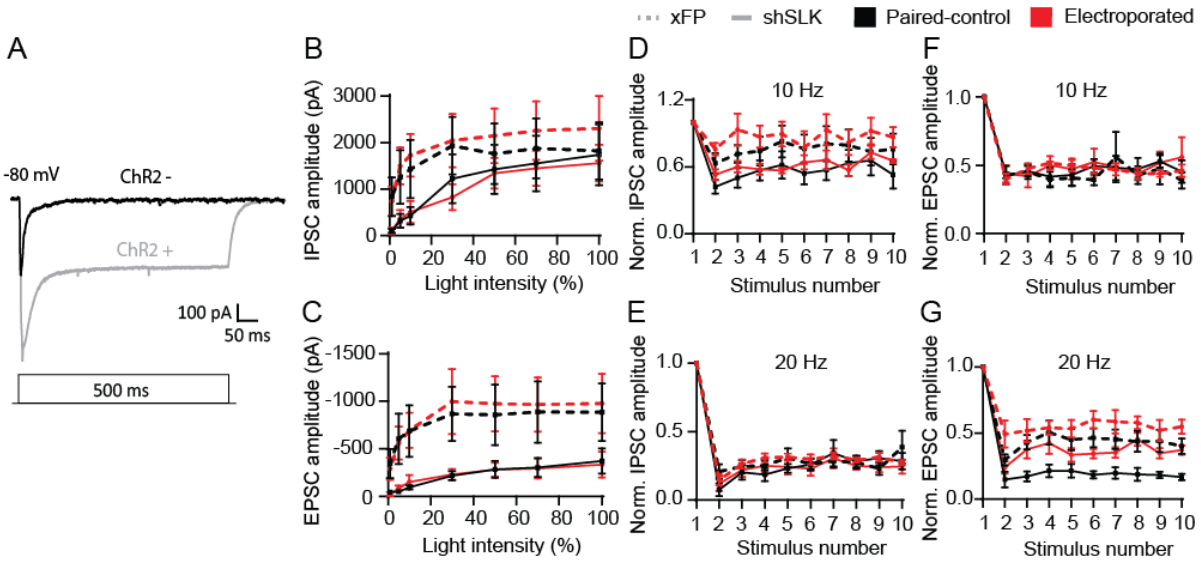


**Figure S3: Feed-back inhibition is not altered in shSLK neurons. A,** Representative synaptic response of cortical neuron not expressing ChR2 (black) after light-based feed-back activation. Neurons displaying long-lasting currents that followed the 500 ms light-pulse (grey) were considered to express ChR2 and were removed from further analysis. **B, C,** Amplitudes of light-evoked feed-back IPSCs (B) and EPSCs (C) across different light stimulation intensities (100% = 20.96 mW light fiber output) in neurons expressing shSLK or control XFP compared to their respective, adjacent paired-control PCs. **D, E,** IPSC amplitudes (normalized to first response) of synaptic responses evoked by light-based stimulation trains at 10 (D) and 20 Hz (E) of ChR2-expressing intracortical axons in neurons expressing shSLK or control XFP compared to their respective, adjacent paired-control PCs. **F, G** As in panels D and E, normalized EPSC amplitudes at 10 (F) and 20 Hz (G). Data are represented as mean ± SEM.

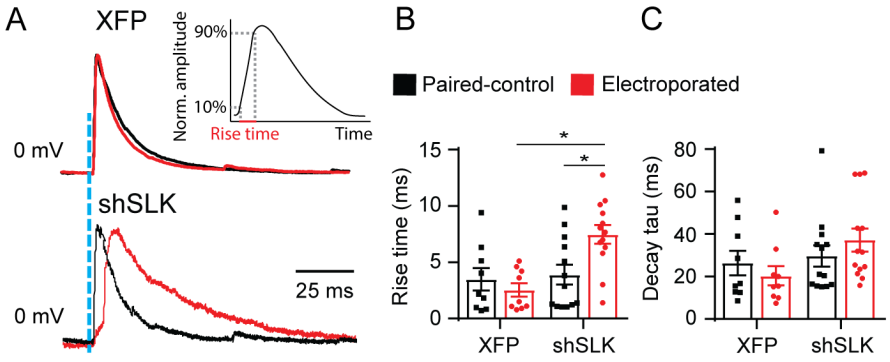


**Figure S4: Kinetics of feed-forward inhibition are altered in SLK-deficient neurons. A,** Representative examples of light-evoked IPSCs in electroporated XFP and shSLK neurons (red traces), and adjacent paired-control PCs in the same slice preparation (black traces). The IPSC amplitude of electroporated cells was normalized to the amplitude of their paired-control cell in order to facilitate kinetics comparisons. Rise time was calculated as the time required for the response to rise from 10% to 90% of its total amplitude (inset plot). **B, C,** Rise time and decay tau quantifications of neurons expressing shSLK (number of pairs = 13) or control XFP (number of pairs = 10) compared to their respective, adjacent paired-control PC. SLK-deficient neurons display a pronounced deficit in feed-forward IPSC rise time. Two-way repeated-measures ANOVA, main effects XFP vs. shSLK: $F_{(1,20)}$=6.412, $p$=0.020; electroporated vs. paired-control: $F_{(1,20)}$=4.005, $p$=0.059; interaction: $F_{(1,20)}$=11.840, $p$=0.003; asterisks in panel B indicate Bonferroni's post-test, shSLK vs. paired-control $p$<0.001, shSLK vs. XFP $p$=0.003). Data are represented as mean ± SEM.

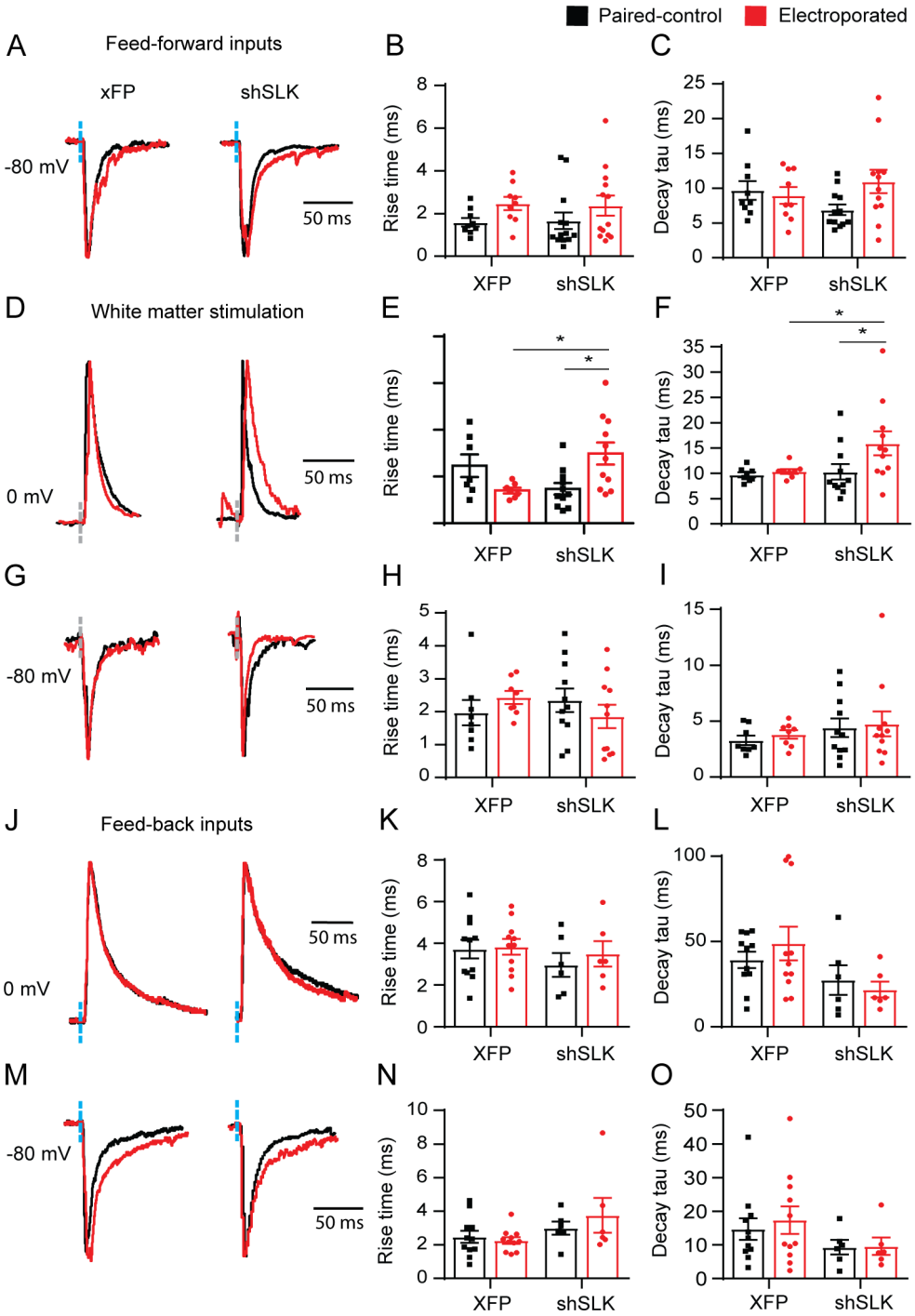


**Figure S5: Kinetics of electrically- and light-evoked PSCs in shSLK neurons. A, D, G, J, M,** Representative examples of PSCs after white matter stimulation (A, EPSCs), light-based feed-forward activation (D, IPSCs; G, EPSCs), and light-based feed-back activation (J, IPSCs; M, EPSCs) in electroporated XFP and shSLK neurons (red traces), and adjacent paired-control PCs (black traces). The PSC amplitudes of electroporated cells were normalized to the amplitude of their paired-control PC in order to facilitate kinetics comparisons. **B, E, H, K, N,** Rise time quantifications of responses after white matter stimulation (B), light-based feed-forward activation (E, H), and light-based feed-back activation (K, N). Asterisks indicate post-tests after two-way repeated-measures ANOVA, rise time (E): Bonferroni's post-test, shSLK vs. paired-control $p$=0.0098, shSLK vs. XFP $p$=0.0150. **C, F, I, L, O,** Decay tau quantifications of responses after white matter stimulation (C), light-based feed-forward activation (F, I), and light-based feed-back activation (L, O). Asterisks indicate post-tests after two-way repeated-measures ANOVA, decay tau (F): Bonferroni's post-test, shSLK vs. paired-control $p$=0.0487, shSLK vs. XFP $p$=0.0243. Data are represented as mean ± SEM.

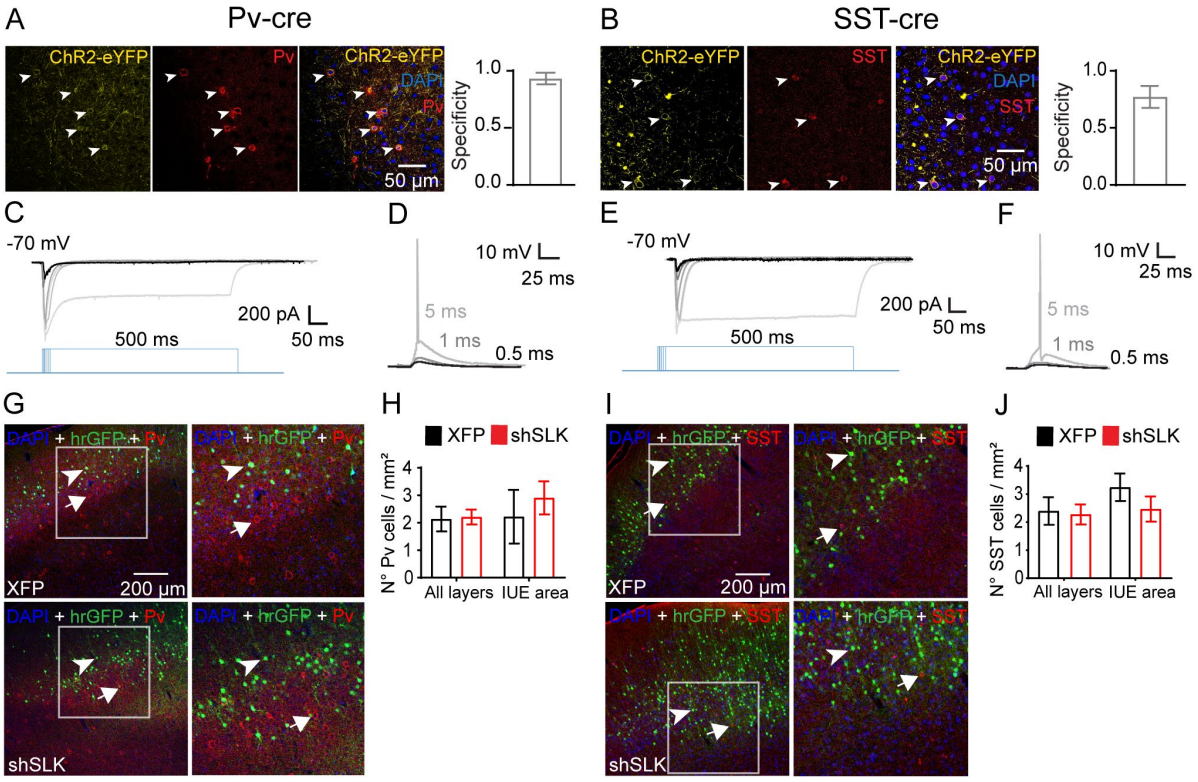


**Figure S6: Optogenetic activation of cortical Pv- and SST-expressing interneurons. A, B,** Immunostaining of Pv (A) and SST (B) in cortical slices from Pv- and SST-cre mice 2 weeks after stereotactic injection of a virus conditionally expressing ChR2. Arrowheads indicate cells expressing ChR2-eYFP and either of the interneuron markers. In panel B, extrasomatic accumulations of intensely fluorescent material that was clearly distinct from the membrane-delimited staining of ChR2-eYFP (arrowheads) and did not have a correlate in the DAPI staining, were not considered as cells and therefore not included in the quantifications (see methods). Bar plots show the fraction of ChR2 positive cells that were also Pv- (A, 0.93 ± 0.05) or SST-expressing cells (B, 0.78 ± 0.11). **C, D, E, F,** Patch-clamp recordings of ChR2-expressing cells in acute slices from Pv- (C) and SST-Cre animals (E) revealed direct photocurrents that increased in amplitude and duration when light stimulation duration was increased. Increasing stimulus duration led to increased depolarization that ultimately resulted in reliable action potential firing in both, PV- (D) and SST-Cre (F) acute slices. **G-J,** Number of PV- and SST-expressing interneurons is not altered in shSLK electroporated animals. **G, I,** Pv (G) and SST (I) immunostaining of cortical slices electroporated with control XFP (upper panels) and shSLK (lower panels). Arrowheads indicate the expression of the IUE plasmids (green), while arrows indicate immunolabeling of PV and SST (red). Note the lack of overlapping between electroporated cells and interneurons. **H, J,** Quantification of the number of Pv- (H) and SST-expressing neurons (J) across all cortical layers and only within the electroporated area. No changes in the number of either interneuron were observed in shSLK electroporated animals. Data are represented as mean ± SEM.

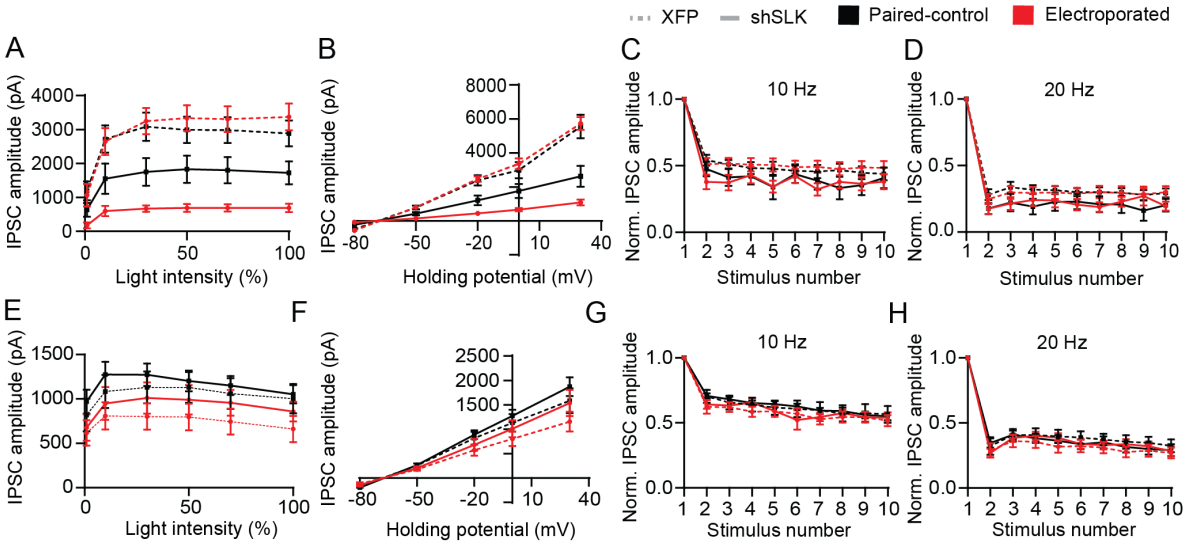


**Figure S7: Pv- but not SST-mediated IPSCs are altered in shSLK neurons. A,** Amplitudes of IPSCs after light-activation of Pv-expressing INs across different stimulation intensities (100% = 20.96 mW light fiber output) in shSLK or XFP electroporated neurons compared to their respective, adjacent paired-control PCs. **B,** Amplitudes of IPSCs after light-activation of Pv-expressing INs across different holding potentials in shSLK or XFP electroporated neurons compared to their respective, adjacent paired-control PCs. shSLK electroporated neurons displayed a robust reduction in Pv-mediated inhibition at different light intensities (A) and holding potentials (B). **C, D,** IPSC amplitudes (normalized to first response) of synaptic responses evoked by light-based stimulation trains of Pv-expressing INs at 10 (C) and 20 Hz (D) in neurons electroporated with shSLK or control XFP compared to their respective, adjacent paired-control PCs. **E,** Amplitudes of IPSCs after light-activation of SST-expressing INs across different stimulation intensities (100% = 20.96 mW light fiber output) in shSLK or XFP electroporated neurons compared to their respective, adjacent paired-control PCs. **F,** Amplitudes of IPSCs after light-activation of SST-expressing INs across different holding potentials in shSLK or XFP electroporated neurons compared to their respective, adjacent paired-control PCs. **G, H,** IPSC amplitudes (normalized to first response) of synaptic responses evoked by light-based stimulation trains of SST-expressing INs at 10 (C) and 20 Hz (D) in neurons electroporated with shSLK or control XFP compared to their respective, adjacent paired-control PCs. Data are represented as mean ± SEM.

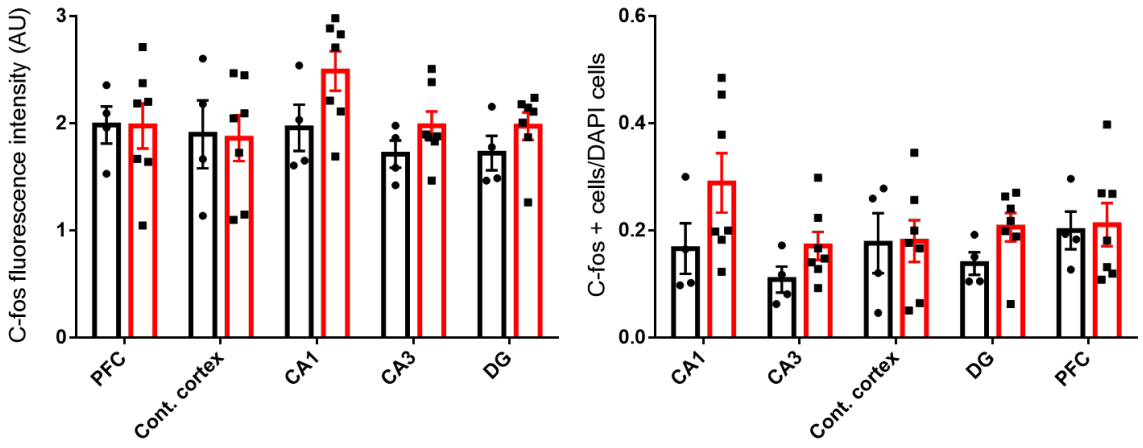


**Figure S8: Quantification of c-fos labelling in prefrontal cortex (PFC), contralateral somatosensory cortex, and the CA1, CA3 and DG subfields of the hippocampus.** Quantification was done similarly as for c-fos in IUE cells, but note that labelling in these areas does not directly compare electroporated and non-electroporated neurons. Left panel shows the normalized average pixel intensity of c-fos labeling quantified in DAPI contours. Contours displaying an average intensity of c-fos signal 3x higher than the average intensity of negative controls were classified as c-fos positive cells and counted (right panel).

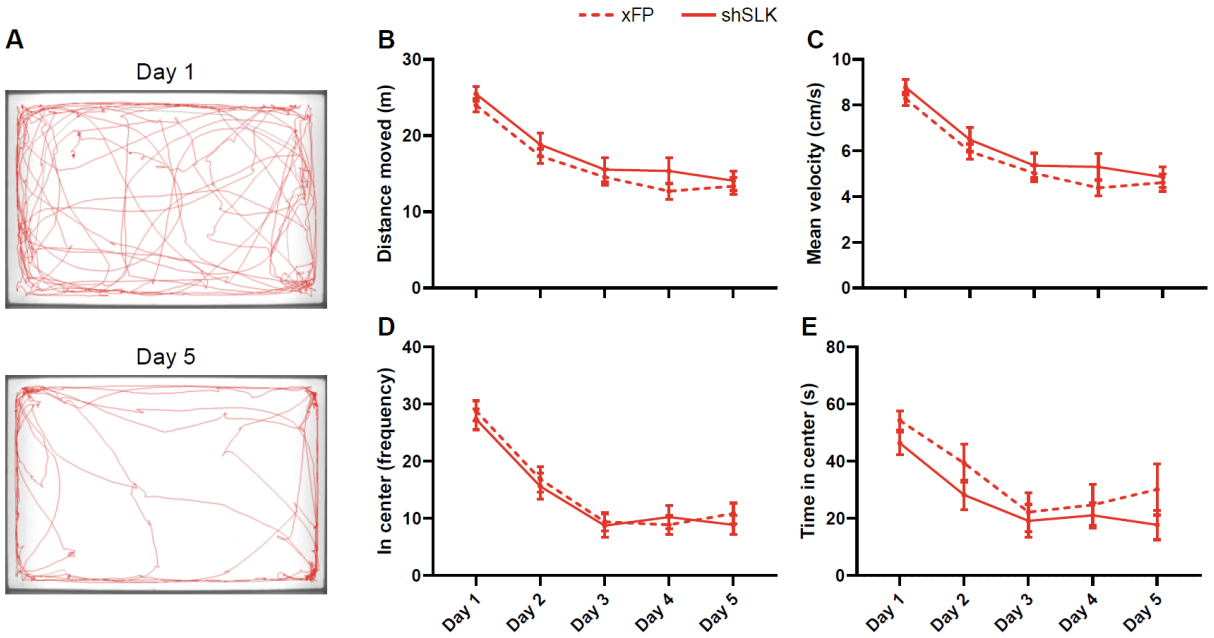


**Figure S9: No changes in open field behaviour in mice electroporated with shSLK. A,** Representative example of open field behavior on day 1 and day 5 of the analysis period (data shown from a control mouse). **B,** Total distance moved during sessions 1-5. **C,** Mean velocity during sessions 1-5. **D, E,** Quantification of how often mice enter the center of the maze (D) and cumulative time spent in the center of the maze (E, center defined as an area 7 cm away from the sides of the open field). Error bars correspond to SEM. N-numbers of panels B-E are 24 sham-control (xFP) mice and 16 shSLK mice. No differences were observed between shSLK and control mice (two-way ANOVA, full results reported in **Table S6**).

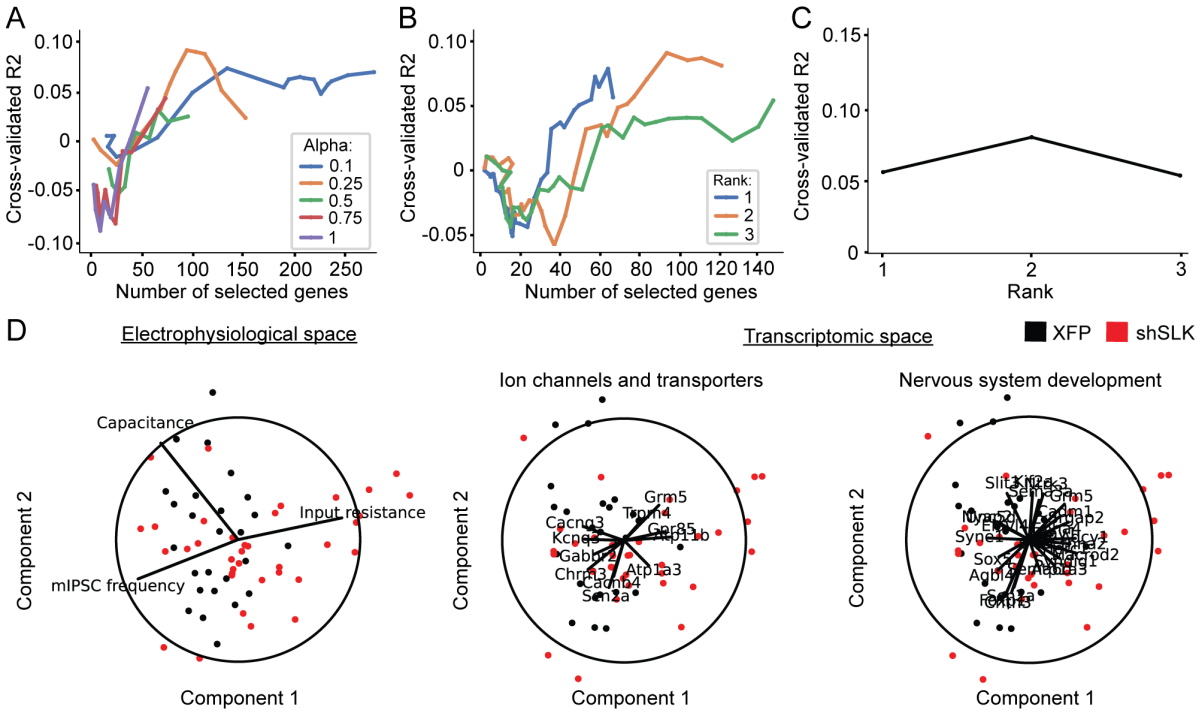


**Figure S10: Cross-validation and additional gene ontology terms for the sparse reduced-rank regression analysis. A,** Cross-validated performance of sparse RRR models for various elastic net penalties (alpha) across different numbers of selected genes. The best performance was found by selecting 113 genes with an alpha value of 0.25. **B,** Cross-validated performance using an alpha value of 0.25 and different numbers of selected genes for different ranks. **C,** Cross-validated performance using an alpha value of 0.25 and selecting 113 genes across different ranks. **D,** Low-dimensional representation of the electrophysiological data (left panel) and the transcriptomic space by using the expression profiles of the 113 genes selected by the sparse RRR model. Genes that encode for ion channels (middle panel) and proteins involved in nervous system development (right panel) were plotted separately to ease visualization.

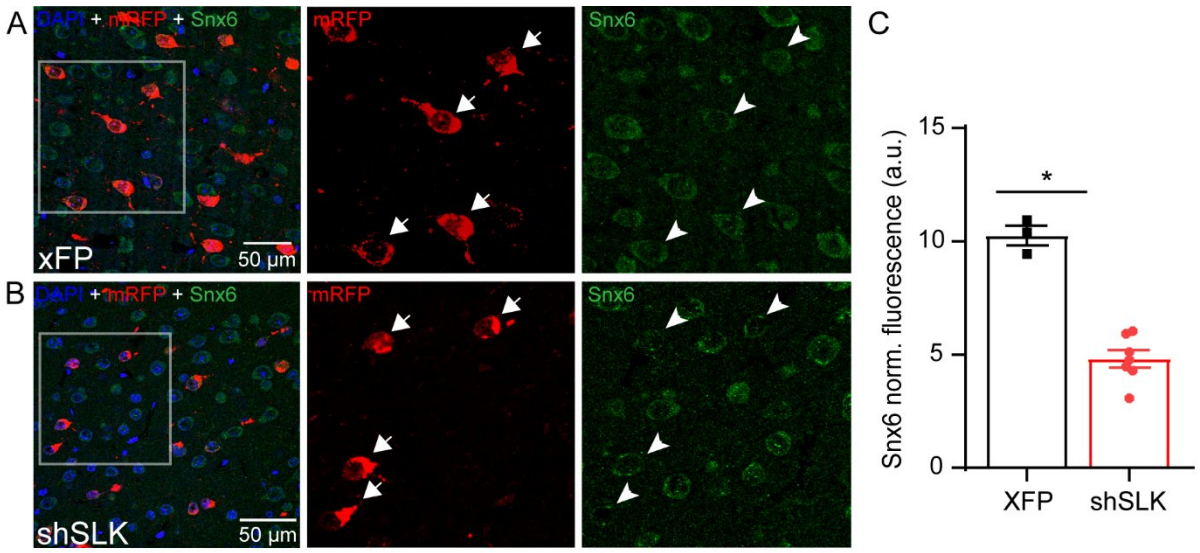


**Figure S11: Snx6 expression in SLK-deficient neurons. A, B,** Snx6 immunostaining of cortical slices electroporated with control XFP (A) and shSLK (B). shSLK electroporated neurons displayed lower levels of Snx6 protein expression (arrowheads)**. C,** Quantification of Snx6 labeling intensity in control XFP and shSLK electroporated neurons. Data points represent averages across all ROIs in an individual animal (XFP = 3; shSLK = 7 mice; quantification done in a total of 838 hrGFP-positive neurons). Asterisks indicate significance in unpaired t-test ($p$<0.0001, panel C, test performed considering N of mice as independent replicates). Data are represented as mean ± SEM.